Shock and Vibration

Nonlinear Dynamics in Drilling Engineering 2021

Lead Guest Editor: Qilong Xue
Guest Editors: Wenjun Huang, Henry Leung, Zhi-Qiao Wang, and Peng Wang

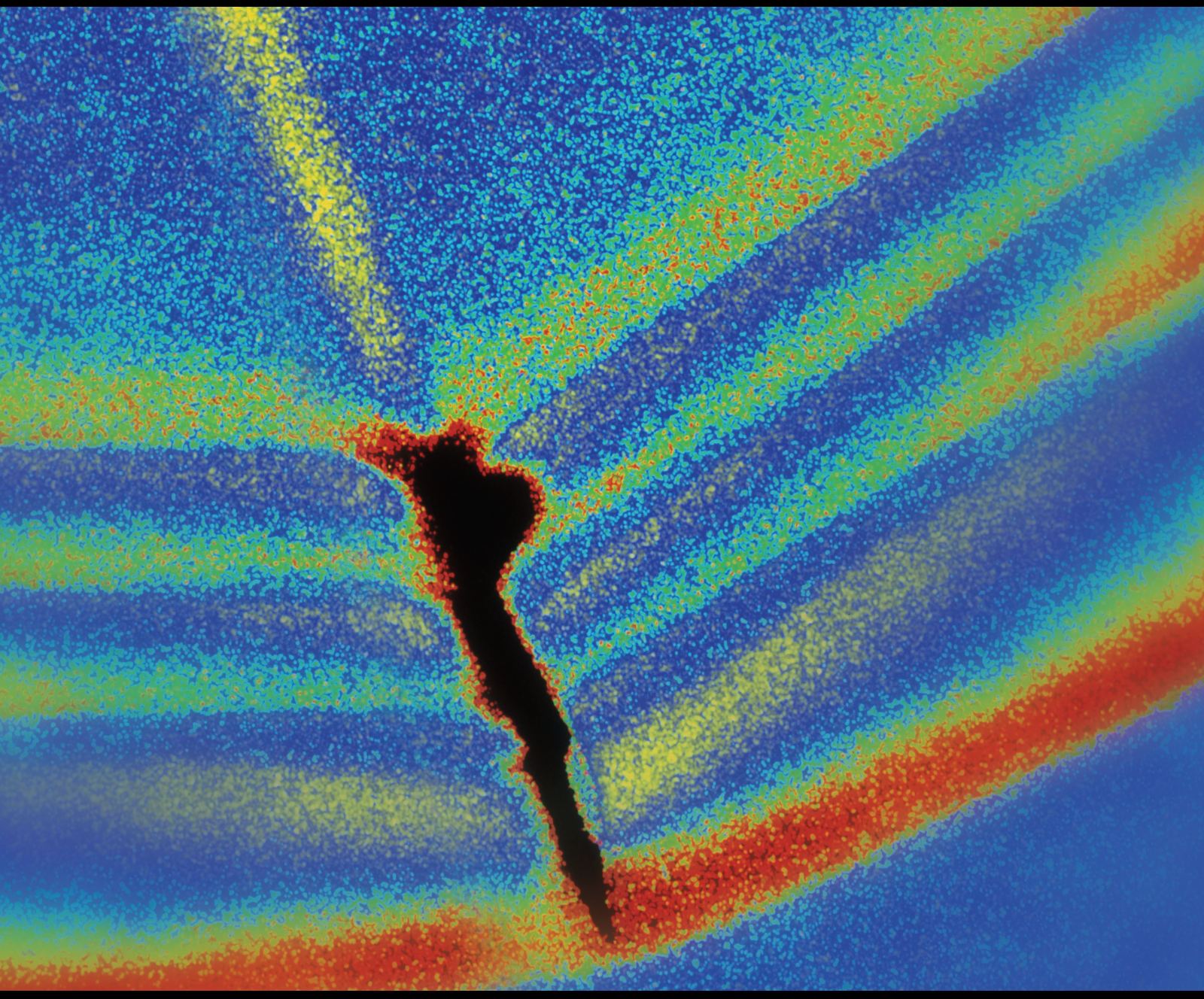

Nonlinear Dynamics in Drilling Engineering 2021

Shock and Vibration

Nonlinear Dynamics in Drilling Engineering 2021

Lead Guest Editor: Qilong Xue
Guest Editors: Wenjun Huang, Henry Leung, Zhi-Qiao Wang, and Peng Wang

Contents

Hindawi
Shock and Vibration
Volume 2022, Article ID 8207899, 10 pages
https://doi.org/10.1155/2022/8207899

Research Article

Study on Dynamics of Hydraulic Control System for Automatic Loading and Unloading of Drill Pipe of Geological Drilling Rig

Zhijian Liu, Yunlong Chen, and Hailong Ruan

Beijing Institute of Exploration Engineering, CGS, Beijing, China

Correspondence should be addressed to Hailong Ruan; rhailong@mail.cgs.gov.cn

Received 5 August 2021; Revised 7 April 2022; Accepted 11 April 2022; Published 21 April 2022

Academic Editor: Qilong Xue

With the increasing demand for resources, the task of the geological survey is growing rapidly. The automatic geological drilling rig, which can improve the efficiency of the geological survey, has become the mainstream development direction. In this study, the hydraulic control system for the automatic screw up and screw down of an automatic drilling rig is studied. Through the establishment of mathematical models such as the four-way slide valve controlled asymmetric cylinder model, drill pipe thread stress model, and steel wire rope elastic model, the hydraulic valve is used to limit the pressure of the hydraulic cylinder, closed-loop control to control rotation speed, and power head floating to prevent screw damage and realize the automatic control of drill pipe up and down of a geological drilling rig. The hydraulic control system is simulated by AMESim software. The simulation model verifies the mathematical model. It is concluded that the maximum transient force of steel wire rope is caused by the elastic coefficient K of steel wire rope, but the magnitude is independent of K. The transient force is the periodic motion force. The displacement, velocity, and acceleration of load are periodic functions related to time. By installing a small flow load sensing valve, the displacement of an asymmetric hydraulic cylinder can be accurately controlled, and then, the displacement of the drilling rig powerhead can be controlled. The combined action of drill pipe speed and power head displacement is adopted, and the power head displacement is followed by PID control through the feedback value of the drill pipe speed, which can realize the automatic loading and unloading of drill pipe and reduce the damage of drill pipe screw during loading and unloading of drill pipe. The research results of this study can provide a theoretical reference and design basis for the follow-up development of an automatic drilling rig.

1. Introduction

Both oil drilling and geological core drilling obtain mineral resources by drilling, and this will still be the main construction method in the next few decades. In the process of drilling, the drill pipe string, as the main drilling mechanism, plays an important role in transmitting force and as a drilling mud channel [1]. Therefore, in order to realize automatic loading and unloading of drill pipes, especially the use of rope-coring drill pipes, there is an insurmountable problem of the screw thread on the drill pipe. When the screw thread is unloaded from the drill pipe, the power head shall be lowered (or lifted) by a pitch while rotating forward (or reverse) one turn. In the process of tightening the thread, the eccentricity of the internal and external threads will cause thread wear or burning, and the insufficient or excessive make-up torque during thread tightening will affect the service life of the joint thread. Most drill pipe thread failures occur from the root of the external thread to the second circle. The main forms of thread failure are wear, root fracture, or longitudinal cracking [2]. Research shows that the failure position of the drill pipe is mainly concentrated in the position of drill pipe joint and thread. In the study of drill pipe stress characteristics, the failure caused by joint thread accounts for about 48% of the total failure of drilling tools [3].

At present, A. R. Shahani and S.M.H. Sharifi [4] have carried out nonlinear finite element contact analysis on threaded structures. Santus C et al. [5] studied the calculation methods of force for hot and cold installation of drill

pipe joint in view of the engineering problems caused by unreasonable screwing up of drill pipe joints. Van Wittenbergh et al. [6] studied the influence of thread contact parameters of the drill pipe joint of the API structure on contact stress by a series of finite element calculation methods and experimental methods and pointed out that the first meshing tooth of male buckle is the most dangerous position for fatigue failure. Croccolo et al. [7] analyzed the causes of joint thread failure of ordinary bolts after torque preloading and the relationship between friction coefficient and make-up torque. Bui et al. [8] established a fatigue life judgment model, which can be used to judge the antifatigue life of large pipe fittings. Research on drill pipe joint thread at home and abroad mainly focuses on the research on thread structure, stress-strain concentration of joint threads, and failure analysis of joint thread. How to prevent and reduce the impact of drill pipe, especially the elastic impact of drill pipe, is also a hot issue in the research of drill pipe drill string [9], but there is little research on the dynamics of the hydraulic control system when the drill pipe thread is screwed on and off.

Starting with the principle of the hydraulic system of loading and unloading drill pipe, this study establishes the four-way slide valve controlled asymmetric cylinder model, the drill pipe thread stress model, and the steel wire rope elastic model, respectively. Taking the parameters of a certain type of drilling rig as the boundary conditions, the dynamics of the hydraulic control system in the process of loading and unloading drill pipe is deeply studied by using simulation software.

2. Closed-Loop Control of Loading and Unloading Drill Pipe

When the automatic drilling rig system completes the process of loading and unloading the drill pipe, it is necessary to realize the screw up and down between the two drill pipes so as to ensure that the drill pipe thread will not be damaged in the process of loading and unloading. When loading and unloading the drill pipe screw thread, the feed oil cylinder shall cooperate with the lifting while the power head rotates to ensure that the power head rotates for one cycle and the feed oil cylinder rises or falls by one pitch.

2.1. Overload Control. The feed cylinder is an actuator that acts on the power head, applies an axial force to the drill pipe, and lifts or lowers the power head. In the process of deep drilling, when the pressure of the feed cylinder is overpressured, the drill pipe will be bent and elastically deformed, resulting in the damage of the drill pipe. At the same time, too high pressure will easily lead to the deviation of the drill bit from the predetermined track.

The feed cylinder outputs pressure or lifting force through hydraulic oil applied to the rod chamber or nonrod chamber. Therefore, the pressure and lifting force can be controlled by controlling the pressure in both chambers of the feed cylinder. The pressure control of the feed cylinder adopts a load-sensitive feedback pressure limit to control the pressure of two chambers of the feed cylinder. Overload control can effectively protect the drill pipe and drill pipe thread buckle.

2.2. Floating Control of Loading and Unloading Drill Pipe. The floating control of loading and unloading drill pipe of the geological drilling rig is mainly to avoid the damage of drill pipe thread caused by the weight of power head when loading and unloading drill pipe. The hydraulic principle is shown in Figure 1. The hydraulic system of the drilling rig power head is composed of main system and floating system. The normal drilling and lifting of the drilling rig are controlled by the main system, and the direction and output flow of the main valve 13 are controlled by the manual proportional pilot valve 16, so as to control the drilling and lifting of the power head and its speed. The safety pressures at the lifting side and the lowering side of the power head are set by the lifting side safety valve 14 and the lowering side safety valve 15, and the balance valve 22 ensures the stability of the power head during lifting, lowering, and hovering.

When the drill pipe is required to make up and break down during tripping, the lifting cylinder of the pipe grabbing manipulator and the feed cylinder of the drill power head need to be matched synchronously with the rotating speed of the drill power head and follow the closed-loop control with the rotating speed of the power head. In the process of drilling rig control, the output shaft of the power head rotates for one cycle, and the power head lifts or lowers a drill pipe pitch to ensure that the drill pipe thread is not affected by the dead weight of the power head. This process is called power head floating control.

The rotary encoder installed at the output shaft of the power head measures the rotation direction and speed of the power head. After collecting the data, the controller compares it with the target direction and speed and controls the valve core displacement of the proportional direction valve 11 by controlling the control current of the electric proportional reducing valve 4 on the lifting side and the electric proportional reducing valve 1 on the pressurizing side of the power head. Then, the output flow and direction of the proportional directional valve are controlled, by controlling the direction and opening of proportional directional valve 11 (flow area, approximately linear ratio with displacement), then controlling the direction and speed of the oil cylinder, finally realizing the follow-up control of power head lifting or lowering, and completing the task of loading and unloading drill pipe.

3. Modeling Analysis

3.1. Four-Way Valve Controlled Asymmetric Cylinder Model. The feed cylinder is a typical four-way spool valve controlled asymmetric hydraulic cylinder. Now, the four-way valve controlled asymmetric hydraulic cylinder is modeled and analyzed to provide a theoretical basis for simulation. The principle of a valve controlled asymmetric hydraulic cylinder is shown in Figure 2.

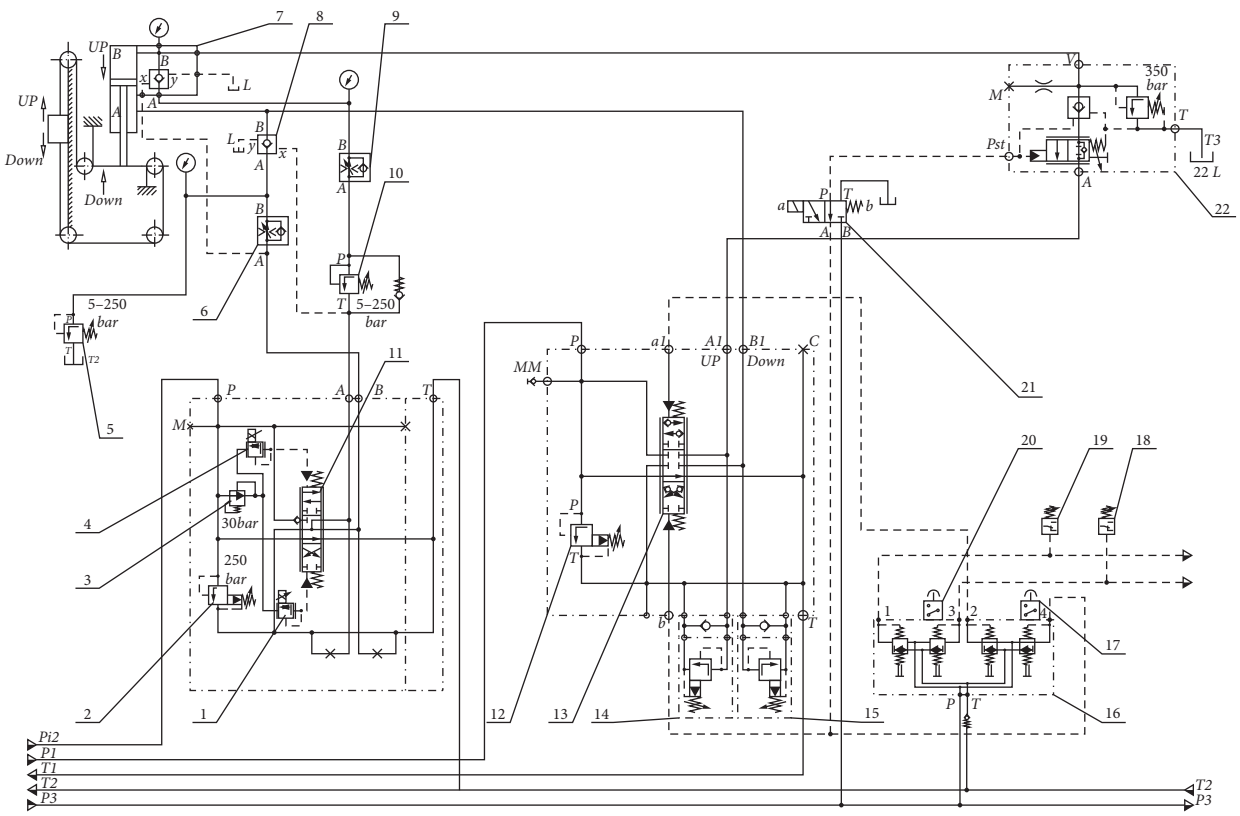

Figure 1: Schematic diagram of power head floating control [10].

The flow equation of the four-way slide valve is shown as

$$
\begin{aligned}
q_{sv1} &= \begin{cases} 0, & x_v < \Delta_1, \\ C_d A_{sv1}\sqrt{\dfrac{2}{\rho}\left(p_s - p_1\right)}, & x_v > \Delta_1, \end{cases} \\
q_{sv2} &= \begin{cases} 0, & x_v < -\Delta_2, \\ C_d A_{sv2}\sqrt{\dfrac{2}{\rho}\left(p_s - p_2\right)}, & x_v > -\Delta_2, \end{cases} \\
q_{sv3} &= \begin{cases} 0, & x_v < \Delta_3, \\ C_d A_{sv3}\sqrt{\dfrac{2}{\rho}\left(p_s - p_3\right)}, & x_v > \Delta_3, \end{cases} \\
q_{sv4} &= \begin{cases} 0, & x_v < -\Delta_4, \\ C_d A_{sv4}\sqrt{\dfrac{2}{\rho}\left(p_s - p_4\right)}, & x_v > -\Delta_4, \end{cases}
\end{aligned}
\tag{1}
$$

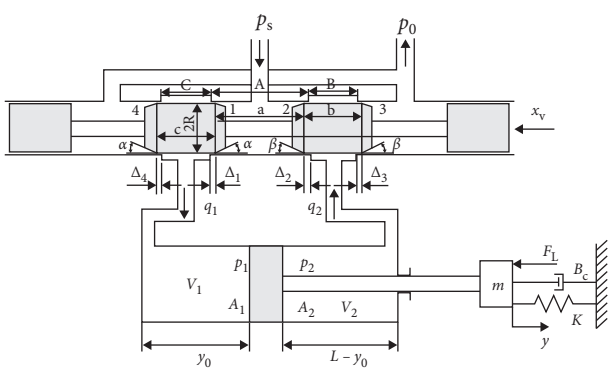

Figure 2: Principle of a four-way valve controlled asymmetric hydraulic cylinder [11].

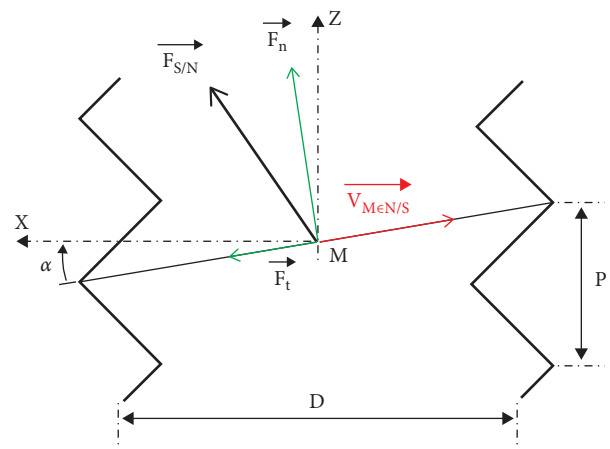

Figure 3: Stress analysis of drill pipe thread.

where C_d is the flow coefficient of the valve, p_s is the valve inlet pressure, q_{svi} is the flow through the ith valve port, $i = 1 \sim 4$, and A_{svi} is the flow area through the ith valve port, $i = 1 \sim 4$.

It can be seen from Figure 2 that the flow in and out of the two chambers of the hydraulic cylinder is shown in following equation:

$$\begin{aligned} q_1 &= f_1(x_v, p_1) = q_{sv1} - q_{sv4}, \\ q_2 &= f_2(x_v, p_2) = q_{sv3} - q_{sv3}. \end{aligned} \tag{2}$$

Equations (3) and (4) are continuity equations of the hydraulic cylinder:

$$\dot{p}_1 = \frac{\beta_e}{V_1(y)}\left[q_1 - C_{ic}(p_1 - p_2) - A_1\dot{y}\right], \tag{3}$$

$$\dot{p}_2 = \frac{\beta_e}{V_2(y)}\left[-q_2 - C_{ic}(p_1 - p_2) - C_{ec}p_2 - A_2\dot{y}\right], \tag{4}$$

where $V_1(y) = A_1(y_0 + y) + V_{d1}$ and $V_2(y) = A_2(L - y_0 - y) + V_{d2}$, L is the stroke of hydraulic cylinder, β_e is the bulk modulus of the working medium, C_{ic} and C_{ec} are internal leakage coefficient and external leakage coefficient, and V_{d1} and V_{d2} are the dead cavity volumes of rodless cavity and rodless cavity independent of stroke.

Equation (5) is the force balance equation of hydraulic cylinder and load:

$$A_1p_1 - A_2p_2 = m\ddot{y} + B_c\dot{y} + ky + F_L, \tag{5}$$

where m is the total mass of piston and load, B_c is the viscous damping coefficient of the piston and load, K is the load spring stiffness, and F_L is the load force.

The mathematical dynamic characteristic equation of valve controlled asymmetric hydraulic cylinder is shown inthefollowing equations:

$$\begin{aligned} \dot{x}_1 &= x_2, \\ \dot{x}_2 &= \frac{1}{m}(A_1x_3 - A_2x_4 - B_cx_2 - kx_1 - F_L), \\ \dot{x}_3 &= \frac{1}{A_1(y_0 + x_1) + V_{d1}}(f_1(x_v, x_3) - C_{ic}(x_3 - x_4) - A_1x_2), \\ \dot{x}_4 &= \frac{1}{A_2(L - y_0 - x_1) + V_{d2}}(-f_2(x_v, x_4) + C_{ic}(x_3 - x_4) - C_{ec}x_4 + A_2x_2). \end{aligned} \tag{6}$$

3.2. Stress Model of Drill Pipe Thread. The stress analysis of drill pipe thread is shown in Figure 3, and the helix angle of drill pipe thread is shown in the following equation:

$$\alpha = \arctan\left(\frac{p}{\pi \cdot D}\right), \tag{7}$$

where p is the pitch and D is the major diameter of the thread.

Equation (8) is the force perpendicular to the thread F_n, which depends on the relative displacement and speed between the nut and the screw:

$$F_n = d.v_{\text{rel}} + k\int v_{\text{rel}}dt, \tag{8}$$

where k is the contact stiffness, d is contact damping, and v_{rel} is the relative linear velocity along the Z-axis.

From equations (9) and (10), the force on nut F_{nut} and the torque on screw T_{screw}:

$$F_{\text{nut}} = F_n \cos\alpha - F_t \sin\alpha, \tag{9}$$

$$T_{\text{screw}} = \frac{D}{2}\left(F_n \sin\alpha + F_t \cos\alpha\right). \tag{10}$$

3.3. Elastic Model of Steel Wire Rope. If the loading force is transmitted by steel wire rope, the steel wire rope has elastic deformation [12]. As shown in Figure 4, (11) is the kinematic equation [13]:

$$\left\{ m_2\ddot{x}_2 - k\left(x_1 - x_2\right) = m_2 g, J_1\ddot{\theta} + k\left(x_1 - x_2\right)r = F_q r, \right. \tag{11}$$

where m_2 is the load mass, x_2 is the load displacement, x_1 is the displacement of steel wire rope, k is the elastic coefficient of steel wire rope, J_1 is the moment of inertia of the pulley, R is the rotation radius of the pulley, F_q is the starting force acting on the pulley, and $M_1 = F_q r$, M_1 is the pulley driving torque.

Equation (12) is the acceleration of steel wire rope:

$$\ddot{x}_1 = \ddot{\theta} r. \tag{12}$$

Combine equations (11) and (12) so that the elastic deformation of steel wire rope, $S = x_1 - x_2$, exports

$$\left\{ m_2\ddot{x}_2 - kS = m_2 g, \frac{J_1}{r^2}\left(\ddot{S} + \ddot{x}_2\right) + kS = F_q. \right. \tag{13}$$

Equation (14) is derived by operation transformation:

$$\ddot{S} + \frac{k\left(J_1/r^2 + m_2\right)}{m_2 J_1/r^2} S = \frac{\left(J_1/r^2 + m_2\right)}{J_1/r^2} m_2 g + F_s \frac{1}{J_1/r^2}, \tag{14}$$

where F_s is the residual force, $Fs = Fq - m2g$:

$$\omega_n^2 = \frac{k\left(J_1/r^2 + m_2\right)}{m_2 J_1/r^2},$$

$$A = \frac{\left(J_1/r^2 + m_2\right)}{J_1/r^2}, \tag{15}$$

$$B = \frac{1}{J_1/r^2},$$

where ω_n is the natural frequency of the system. Then, equation (15) is obtained from equation (14):

$$\ddot{S} + \omega_n^2 S = A m_2 g + B F_s. \tag{16}$$

The kinematics equation of the system is obtained by solving equation (15), including displacement equation (16), velocity equation (17), and acceleration equation (18):

$$S = A \sin\omega_n t + B \cos\omega_n t + \frac{m_2 F_s}{k\left(m_2 + J_1/r^2\right)} + \frac{m_2 g}{k}, \tag{17}$$

$$\ddot{S} = A\omega_n \cos\omega_n t - B\omega_n \sin\omega_n t, \tag{18}$$

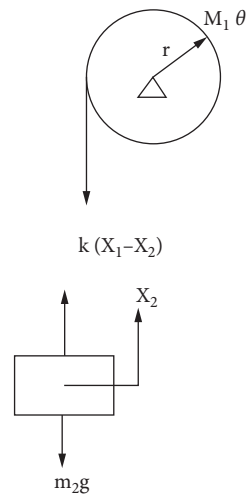

Figure 4: Suspension model of elastic steel wire rope.

$$\ddot{S} = -A\omega_n^2 \sin\omega_n t - B\omega_n^2 \cos\omega_n t. \tag{19}$$

When $t = 0$, it is the initial start; equations (19) and (20) are obtained:

$$S = \frac{m_2 g}{k},$$
$$\ddot{S} = 0, \tag{20}$$

$$A = 0,$$
$$B = -\frac{m_2 F_s}{k\left(m_2 + J_1/r^2\right)}. \tag{21}$$

Therefore, equations (16), (17), and (18) become equations (21), (22), and (23):

$$S = \frac{m_2 F_s}{k\left(m_2 + J_1/r^2\right)}\left(1 - \cos\omega_n t\right) + \frac{m_2 g}{k}, \tag{22}$$

$$\ddot{S} = \frac{m_2 F_s}{k\left(m_2 + J_1/r^2\right)}\omega_n \sin\omega_n t, \tag{23}$$

$$\ddot{S} = \frac{m_2 F_s}{k\left(m_2 + J_1/r^2\right)}\omega_n^2 \cos\omega_n t. \tag{24}$$

The kinematic equations of displacement, velocity, and acceleration of load obtained from equation (13) are equations (24), (25), and (26):

$$x_2 = \frac{F_s}{\left(m_2 + J_1/r^2\right)}\frac{t^2}{2} - \frac{F_s}{\left(m_2 + J_1/r^2\right)}\frac{1}{\omega_n}\left(1 - \cos\omega_n t\right), \tag{25}$$

$$\ddot{x}_2 = \frac{F_s}{\left(m_2 + J_1/r^2\right)}\left(t - \frac{1}{\omega_n}\sin\omega_n t\right), \tag{26}$$

$$\ddot{x}_2 = \frac{F_s}{\left(m_2 + J_1/r^2\right)}\left(1 - \cos\omega_n t\right). \tag{27}$$

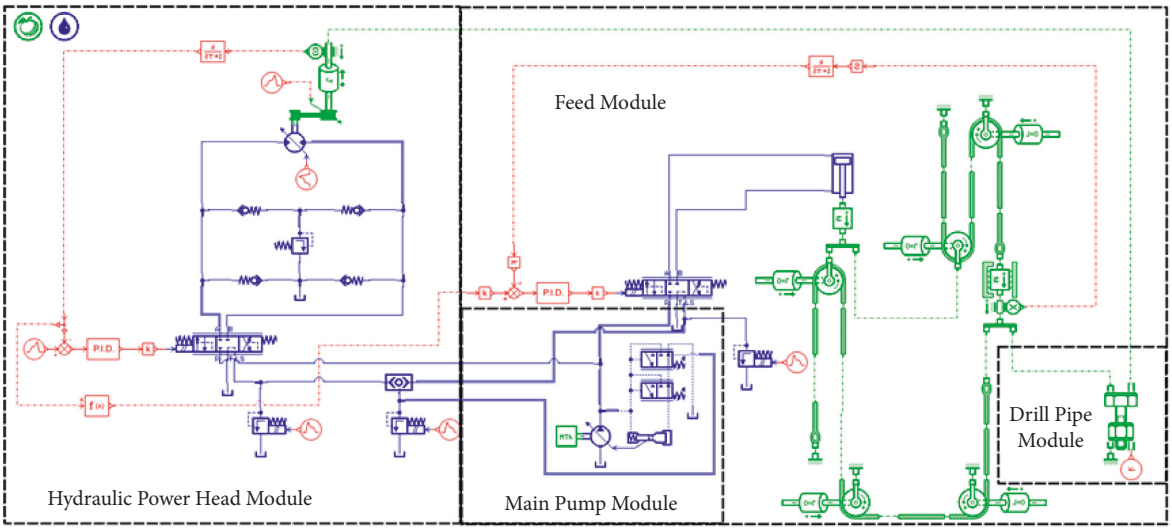

Figure 5: Simulation model of loading and unloading drill pipe.

Table 1: Simulation boundary parameters of the hydraulic system of the geological drilling rig.

NO.	Parameter name (unit)	The set value
1	Maximum pressure of main pump (MPa)	35
2	Engine speed (r/min)	2400
3	Auxiliary pump displacement (mL/r)	32
4	Main pump displacement (mL/r) [15]	74
5	Volumetric efficiency of main pump [15]	0.92
6	Main pump mechanical efficiency [15]	0.95
7	Volumetric efficiency of auxiliary pump	0.8
8	Auxiliary pump mechanical efficiency	0.95
9	Feed cylinder diameter (mm)	90
10	Feed cylinder rod diameter (mm)	70
11	Feed cylinder stroke (mm)	1125
12	Maximum displacement of power head motor (mL/r) [14]	80.4
13	Minimum displacement of power head motor (mL/r)	40
14	Pressure difference between inlet and outlet of power head motor (MPa)	24
15	Power head motor 1 stage reduction ratio I_0	2.5
16	Power head 1 gear reduction ratio i_1	15.625
17	Power head 2 gear reduction ratio i_2	7.8125
18	Power first 3 gear reduction ratio i_3	4.3925
19	Power first 4 gear reduction ratio i_4	2.5
20	Power head motor volume efficiency [14]	0.95
21	Power head motor mechanical efficiency [14]	0.98
22	Mechanical efficiency of power head reducer [14]	0.98

Equation (27) is the transient force F_2 of steel wire rope:

$$F_2 = kS = \frac{m_2 F_s}{\left(m_2 + J_1/r^2\right)}\left(1 - \cos\omega_n t\right) + m_2 g. \tag{28}$$

When,cos $\omega_n t = -1$, $F_2 = F_{2\max}$, and

$$F_{2\max} = 2\frac{m_2 F_s}{\left(m_2 + J_1/r^2\right)} + m_2 g. \tag{29}$$

Table 2: PID parameters in the simulation model.

Module	P	I	D
Hydraulic power head module PID	100	0	2
Feed module PID	100	0	1

According to (28), the maximum transient force $F_{2\max}$ of the steel wire rope is caused by the elastic coefficient k of the steel wire rope, but the magnitude is independent of k. The transient force F_2 is a periodic motion force.

The displacement, velocity, and acceleration of load are periodic functions related to time.

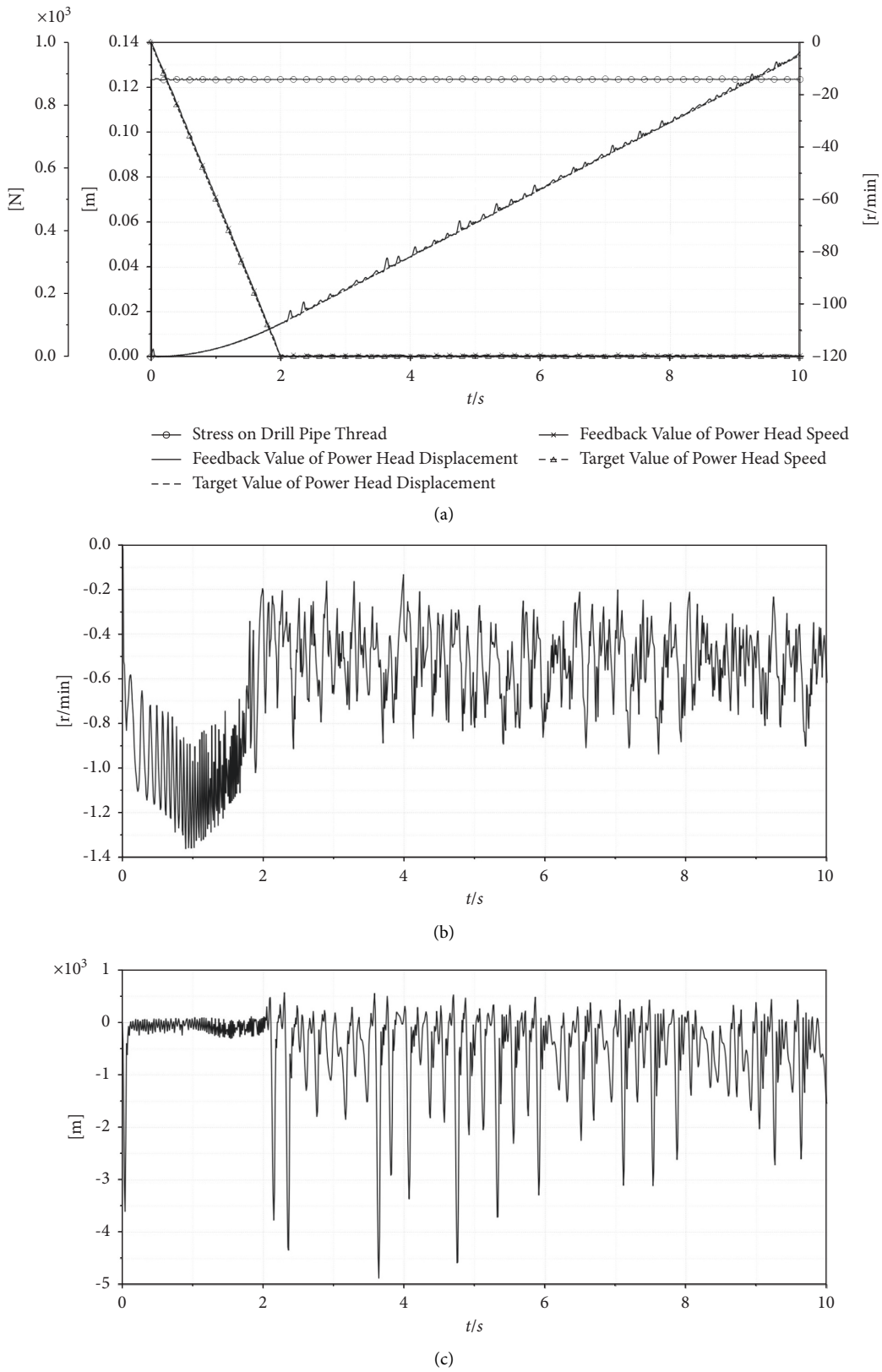

Figure 6: Simulation curve of loading and unloading drill pipe. (a) Simulation curve of loading and unloading drill pipe. (b) Error curve of powerhead speed. (c) Error curve of dynamic head displacement.

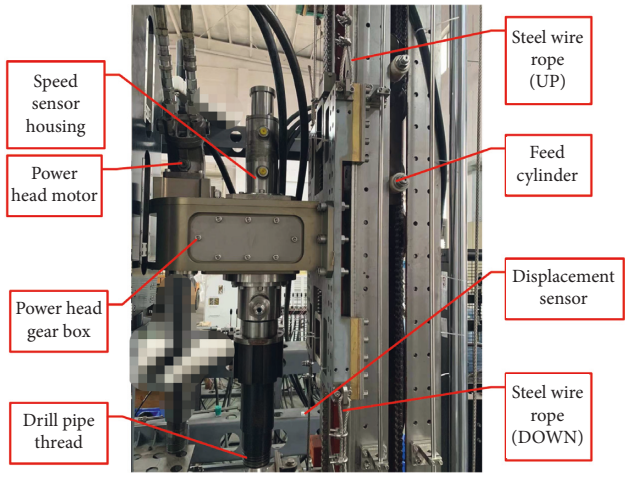

Figure 7: Application in subsea drilling rig.

Table 3: List of sensor parameters.

Sensor name	Measurement parameters	Signal output type	Sensor accuracy	Sensor shape
Incremental encoder	Rotate speed	Pulse frequency	360ppr	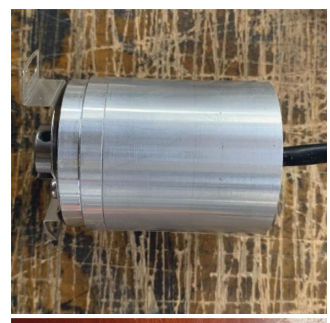
Displacement sensor	Displacement	4–20 mA	0.05% range	

4. Research on Modeling and Simulation

Using the established mathematical model, the AMESim model shown in Figure 5 is established according to the principle of Figure 1, and the simulation parameters are set according to the boundary of Table 1.

The loading and unloading drill pipe is simulated by AMSIM software. The power head speed control is the main control, and the feed cylinder control is the follow-up control. A PID controller [16, 17] is adopted for the speed and displacement of power head. The speed feedback value is converted into the displacement variable value of the power head by the controller and input into the PID controller of the feed cylinder. The displacement of the feed cylinder is controlled by the auxiliary valve. The PID parameters in Figure 5 are shown in Table 2.

It can be seen from Figure 6 that the power head drives the drill pipe from static to rotating speed of 120r/min, and the rotating speed is stable, as shown in Figure 6(a). The speed control error is small, as shown in Figure 6(b). Affected by the elasticity of the steel wire rope, the displacement of the power head fluctuates periodically, as shown in Figure 6(c), and the displacement error curve of the power head, which is consistent with the kinematic equation of the steel wire rope elastic model, but has little effect on the force on the drill pipe thread, and the drill pipe thread is only affected by the gravity of the drill pipe. The simulation shows that the small flow valve core of the auxiliary valve can realize the closed-loop control of the screw thread loading and unloading drill pipe and avoid the screw thread damage caused by the control error through the connection of the steel wire rope, and the steel wire rope plays an elastic buffer role.

5. Practical Application

Applying the theory and scheme of this study on a 20m subsea drilling rig and using the compound action of power

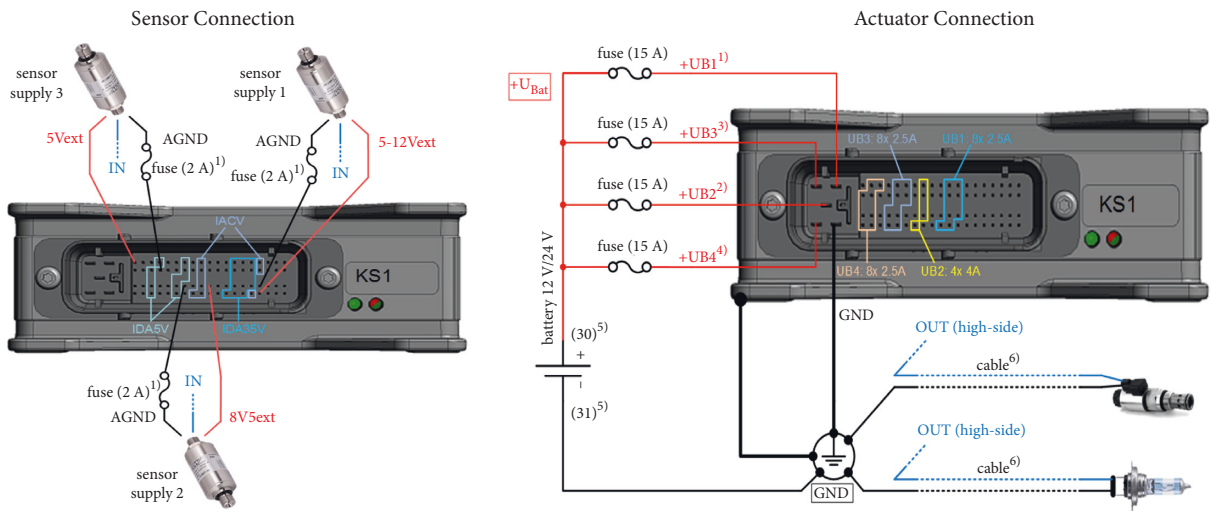

Figure 8: Wiring diagram of sensor and electric proportional valve [18].

head output drill pipe speed and power head displacement, through the drill pipe speed sensor and power head displacement sensor installed on the output side of the power head, as shown in Figure 7, the following control of power head displacement during drill pipe up and down is realized to effectively reduce the damage of drill pipe thread buckle.

The incremental encoder is selected to measure the drill pipe speed on the output side of the power head and installed in the speed sensor housing to prevent damage by seawater pressure. High precision pull wire displacement sensor is selected to measure the up and down displacement of the power head, and the encoder is encapsulated. The sensor parameters are shown in Table 3.

ESX-3CM special controller for construction machinery is selected for sensor signal acquisition and electric proportional valve control to build a closed-loop control. The sensor and electric proportional valve can be directly connected with the ESX-3CM controller, and the wiring mode is shown in Figure 8.

The ESX-3CM is a control and measurement unit. It is a control unit for managing sensors and actors within your system. The ESX-3CM is a control unit that consists of a modern and capable 32-bit architecture based on the TriCore TC1798 processor. The configured hardware is optimized for applications within mobile machines. Up to a total of 56 analog/digital input and outputs for measure and control is available for challenging tasks. [18].

6. Conclusion

In this study, the dynamics of drill pipe up and down shackle of the automatic geological drilling rig is studied. Starting from the hydraulic control system, the problem of thread buckle damage caused by excessive power head weight of geological drill pipe up and down shackle can be solved. The following conclusions can be drawn:

(1) The maximum transient force $F_{2\max}$ of the steel wire rope is caused by the elastic coefficient k of the steel wire rope, but the magnitude is independent of k. The transient force F_2 is a periodic motion force. The displacement, velocity, and acceleration of load are periodic functions related to time.

(2) The installation of a small flow load-sensitive valve can accurately control the displacement of asymmetric hydraulic cylinder and then control the displacement of the power head. It has been well applied and verified in the subsea drilling rig project.

(3) The combined action of drill pipe speed and power head displacement is adopted, and the power head displacement is followed and controlled through drill pipe speed feedback. Combined with the feeding and loading of the drill rig power head, the steel wire rope is used to transfer the loading force, which can realize the automatic loading and unloading of drill pipe and effectively reduce the damage of drill pipe thread buckle.

Data Availability

The data in the tables used to support the findings of this study are included within the article. The data in the figures used to support the findings of this study are available from the author (lzjcumtb@126.com) upon request.

Conflicts of Interest

The authors declare that they have no conflicts of interest.

References

[1] H. X. Shi, *Research on Thread Structure of Drill Pipe Connection*, China University of Geosciences, Beijing, China, 2017.

[2] C. Cai, *Stress Simulation Analysis and Gas-Sealing Capacity Researching of Casing Threaded Connection*, China University of Geosciences, Beijing, China, 2016.

[3] W. Y. Wang, Y. X. Tang, and M. F. Zhu, *Drill Collar Thread Failure Analysis and Settle Measures*, Oil Field Equipment, Beijing, China, 2007.

[4] A. R. Shahani and S. M. H. Sharifi, "Contact stress analysis and calculation of stress concentration factors at the tool joint of a drill pipe," *Materials & Design*, vol. 30, no. 9, pp. 3615–3621, 2009.

[5] C. Santus, L. Bertini, M. Beghini, A. Merlo, and A. Baryshnikov, "Torsional strength comparison between two assembling techniques for aluminium drill pipe to steel tool joint connection," *International Journal of Pressure Vessels and Piping*, vol. 86, no. 2-3, pp. 177–186, 2009.

[6] J. Van Wittenbergahe, P. De Baets, W. De Waele, and S. Van Autreve, "Numerical and experimental study of the fatigue of threaded pipe couplings," in *Proceedings of the 9th International Conference on Surface Effects and Contact Mechanics: Computational Methods and Experiments*, pp. 163–174, WIT Press, Southampton, UK, June 2009.

[7] D. Croccolo, M. De Agostinis, and N. Vincenzi, "Failure analysis of bolted joints: effect of friction coefficients in torque-preloading relationship," *Engineering Failure Analysis*, vol. 18, no. 1, pp. 364–373, 2011.

[8] T. T. Bui, G. De Roeck, J. Van Wittenberghe, E. Reynders, P. De Baets, and W. De Wim, "A modal approach to identify fatigue damage in threaded connections of large scale tubular strucures," in *Proceedings of the Internaional Conference on Noise and Vibration Engineering*, ISMA, Leuven, Belgium, July 2011.

[9] S. X. Bai, ZH. J. Liu, and J. Wang, "Research on the dynamics of geological drilling rig against drill pipe impact," *Hindawi.Shock and Vibration.*vol. 2021, Article ID 6679169, 19 pages, 2021.

[10] ZH. J. Liu, *Research on Dynamic Characteristics of Working Device ofAutomatic Geological Drillig Rig Pipe Handling Systems*, China University of Geosciences, Beijing, China, 2019.

[11] H. E. Merritt, *Hydraulic Control System*, John Wiley & Sons, Hoboken, NJ, USA, 1967.

[12] M. J. Zhang and Q. Cao, *Dynamics of Construction Machinery*, National Defense Industry Press, Beijing, China, 2012.

[13] Q. Y. Liu, Q. H. Meng, and D. X. Pang, *Research and Application of Drilling System Dynamics Simulation*, Science Press, Beijing, China, 2009.

[14] Bosch Rexroth Company, *Mobile Machinery Hydraulic-Product Catalog-Part II-Hydraulic Motor-Reducer*, BoschRexroth Company, Lohra Main, Germany, 2014.

[15] Bosch Rexroth Company, *Mobile Machinery Hydraulic-Product Catalog-Part I-Hydraulic Pump*, Bosch Rexroth Company, Lohra Main, Germany, 2014.

[16] Bosch Rexroth Company, *Mobile Machinery Hydraulic-Product Catalog-Part III-Mobile Machinery Control Device*, Bosch Rexroth Company, Lohra Main, Germany, 2014.

[17] Z. J. Liu, B. L. Liu, and Y. B. Hu, *Fault Simulation of Hydraulic Winch System Stall. Hydraulic and Pneumatic*, Beijing, China, 2016.

[18] Sensor-Technik Wiedemann GmbH, *ESX-3CM CODESYS V3 User Manual*, Sensor-Technik Wiedemann, Kaufbeuren, Germany, 2017.

Hindawi
Shock and Vibration
Volume 2021, Article ID 2764803, 12 pages
https://doi.org/10.1155/2021/2764803

Research Article

Experimental Study on the Transition between Static and Kinetic Frictions of Steel/Shale Pairs

Qin Lian,[1] **Chunxu Yang**,[1] **and Jifei Cao**[2]

[1]*Technical Development Department, Sinopec Shengli Petroleum Engineering Co., Ltd., Dongying 25700, China*
[2]*Drilling Technology Research Institute, Sinopec Shengli Petroleum Engineering Co., Ltd., Dongying 25700, China*

Correspondence should be addressed to Chunxu Yang; spring.sun@163.com

Received 13 September 2021; Accepted 6 October 2021; Published 11 November 2021

Academic Editor: Peng Wang

The transition between static and kinetic frictions of steel/shale pairs has been studied. It was found that the coefficient of friction decreased exponentially from static to dynamic friction coefficient with increasing sliding displacement. The difference between static and dynamic friction coefficients and the critical distance D_c under the dry friction condition is much larger than that under the lubricated condition. The transition from static to dynamic friction coefficient is greatly affected by the normal load, quiescent time, and sliding velocity, especially the lubricating condition. Maintaining continuous lubrication of the contact area by the lubricant is crucial to reduce or eliminate the stick-slip motion. The results provide an insight into the transition from static to dynamic friction of steel/shale pairs.

1. Introduction

Slide drilling with a bent-housing motor dominates the directional market of the petroleum and natural gas drilling industry [1]. The drill string with a length of thousands of meters slides along the axial direction inside the cylindrical borehole wall at a very low speed (0.1–1 mm/s); at the same time, stick-slip between the drill string and borehole wall occurs frequently due to the transition between static and kinetic frictions and the velocity weakening of the friction coefficient. The friction model which only considers a constant dynamic friction coefficient (such as the Coulomb model) used for rotary drilling is inapplicable in slide drilling. On the contrary, the accurate value of friction force between the drill string and borehole wall under the sliding drilling condition is the basis data for designs of well track and tool face adjusting and is the bond between data at the wellhead and bottom of the well, which is also the key issue to realize intelligent drilling [2, 3]. Thus, the friction coefficient between the drill string and borehole wall is a new and very important problem that needs to be resolved immediately.

A number of studies on stick-slip motion in a low-velocity regime, caused by the time dependence of static friction, the transition between static and kinetic frictions, and the velocity weakening of the friction coefficient, have been carried out. Several friction models have been formulated in terms of friction coefficients as a function of the relative sliding velocity, displacement, and quiescent time [4–13], which can be categorized as physics-based [14–17] and phenomenological [18–21]. Phenomenological friction models include static [18] and dynamic models [22–24]. Static models are usually described as a function of relative velocity, such as the well-known Coulomb and Stribeck models, and can capture the drooping characteristic but hysteretic behavior of the friction force. The friction force of dynamic models depends on internal states along with the relative velocity of the contacting surfaces, such as the well-known Dahl [25] and RSF (rate and state friction) models, and can capture hysteretic behaviors of the friction force at the same time. In particular, RSF model has been very successful in describing macroscale friction for many materials, including rocks [26–31]. In the petroleum and natural gas drilling industry, Coulomb friction model was adopted to calculate the friction force between the drill string and borehole wall in the last few decades, and the Stribeck model [32], Dahl model [33], and self-contained friction model [34] were used with the application of technology of

friction reduction by vibrating the drill string until a few years ago. The introduction of these models considers the effect of stick-slip motion of the drill string on friction to a certain extent; however, the characteristics of low velocity, stick-slip, and complex lubricating condition of the relative motion between the drill string and borehole wall make it difficult for the friction model related to velocity and quiescent time to play a role, and the more complex the model is, the more difficult it is to identify its parameters. The friction model, as a function of the relative sliding displacement, is more suitable for the operating condition in the petroleum and natural gas drilling industry.

The critical distance (D_c) is understood to be the elastic deformation necessary to break the contact between asperities, formed during static contact of the interface materials, where the static friction coefficient persists before it steadily decreases to the kinetic one [35], and varies for different rubbing pairs [36, 37]. Tian et al. [38] carried out nanoscale experiment to account for the activation and passivation of chemical reaction sites and the formation of new chemical bonds from dangling bonds during sliding, and results showed D_c is sensitive to the surface chemistry and nearly independent of sliding velocity. Li et al. [39] performed aging experiments for single-asperity silica-silica nanocontacts to isolate the physical mechanisms and found the static friction increased logarithmically with time for hold times from 0.1 to 100 s in the absence of plastic deformation of the contact, which strongly supported chemical bond formation as the operative aging mechanism. Mitchell et al. [37] investigated the frictional properties of gabbro under low normal stress, dry, and hydrated conditions and found that slip becomes increasingly more unstable (velocity weakening) with increasing temperature. Thus, the transition from static to dynamic friction coefficient and the critical distance for different rubbing pairs are influenced by many factors and difficult to be determined by the theoretical arithmetic.

The aim of the present paper was to study the transition law from static to kinetic friction and the critical distance of steel/shale pairs under unlubricated or oil-lubricated conditions. This paper is organized as follows: the setup and procedure of the experiment are described in Section 2, and the surface morphology and mechanical parameters of the steel/shale pair were measured through the nanometer indentation method. The effects of normal load, quiescent time, sliding velocity, and lubricated condition on the transition from static to dynamic friction coefficient are shown and analyzed in Section 3. The microscopic wear and materials' transfer of the steel/shale specimens are, respectively, scanned and measured in Section 4 to analyze the reason for the transition between static and dynamic frictions.

2. Experimental Details

2.1. Setup and Procedure. The coefficients of static and dynamic frictions and their transition were measured by using a specially designed ball-on-rectangular solid friction tester shown in Figure 1. The steel ball (13 mm-diameter balls of 35CrMo) and shale were used as the sliders in the tribological tests. The shale specimens were collected from an outcrop of the Lower Silurian Longmaxi Formation at the Sichuan Basin in southwestern China, which is the most significant exploration area for unconventional gas in China. The steel ball specimen was attached to a rigid square box and pressed by dead weights of 22 or 38 N, respectively, against the rectangular solid shale specimen. The tangential force (F_T) acquisition began after applying the normal load, and the steel ball slid along the axial direction of the screw rod with speed V until the terminal of single trip and slid backward after resting for 0, 1, 5, 30, and 60 s, respectively. Repeat this process until the experimental set time was over. From the resulting F_T versus time, the static coefficient of friction μ_s was determined as the ratio of tangential force at the onset of relative sliding divided by the applied normal load. After the transition from static to kinetic friction, relative sliding occurred generally with the velocity of 22.78, 85.72, and 266.67 μm/s, respectively. The kinetic coefficient of friction μ_k was determined as the ratio of tangential force at the steady relative sliding divided by the applied normal load. For more details about the experimental setup, refer to [40].

Before each test, the specimens were cleaned in an ultrasonic bath with isopropanol. Unlubricated tests were run in the laboratory air at a room temperature of 20°C and the relative humidity of 64%. In the lubricated tests, additive-free mineral oil was fed into the contact area before the ball and the plate were mated, and the viscosity of oil is $\eta_{20°C} = 0.294$ Pa·s and $\eta_{40°C} = 0.085$ Pa·s.

2.2. Materials. In order to obtain the surface quality of specimens, white light interferometry and electron microscope scanning were conducted for the commercially available steel ball and the polished shale before tests. The shale specimens were finished by sandpaper with 400, 1200, and 3000 meshes under a normal force of 10 N during 20 s, respectively. The roughness value R_a of the steel ball equals 0.20 μm. Figure 2 shows the scanning electron micrographs of three shale surfaces. The surface morphology parameters of the shale samples, including R_a (arithmetic average roughness), R_{pk} (height and portion of asperity peaks), and R_k and R_{vk} (depth and portion of cavities on the machined surface, respectively), before tests are shown in Table 1.

The contact between the real rough surface is usually a mixed elastoplastic system. The plasticity index, ψ, was computed for both contacting surfaces in order to describe the deformation properties of the contacting asperities. Whitehouse [41] proposed a plasticity index defined by

$$\psi = \frac{E'}{H}\sqrt{\frac{R_q}{R}}, \tag{1}$$

$$\frac{1}{E'} = \frac{1-\nu_1^2}{E_1} + \frac{1-\nu_2^2}{E_2}, \tag{2}$$

where ψ is the plasticity index, the contact deformation is fully elastic when $\psi < 0.6$, fully plastic when $\psi > 10$, and elastoplastic when $1 < \psi < 10$; E' is the composite modulus of elasticity, MPa; H is the Brinell hardness of materials, MPa; R_q is the root-mean-square roughness of surface asperities,

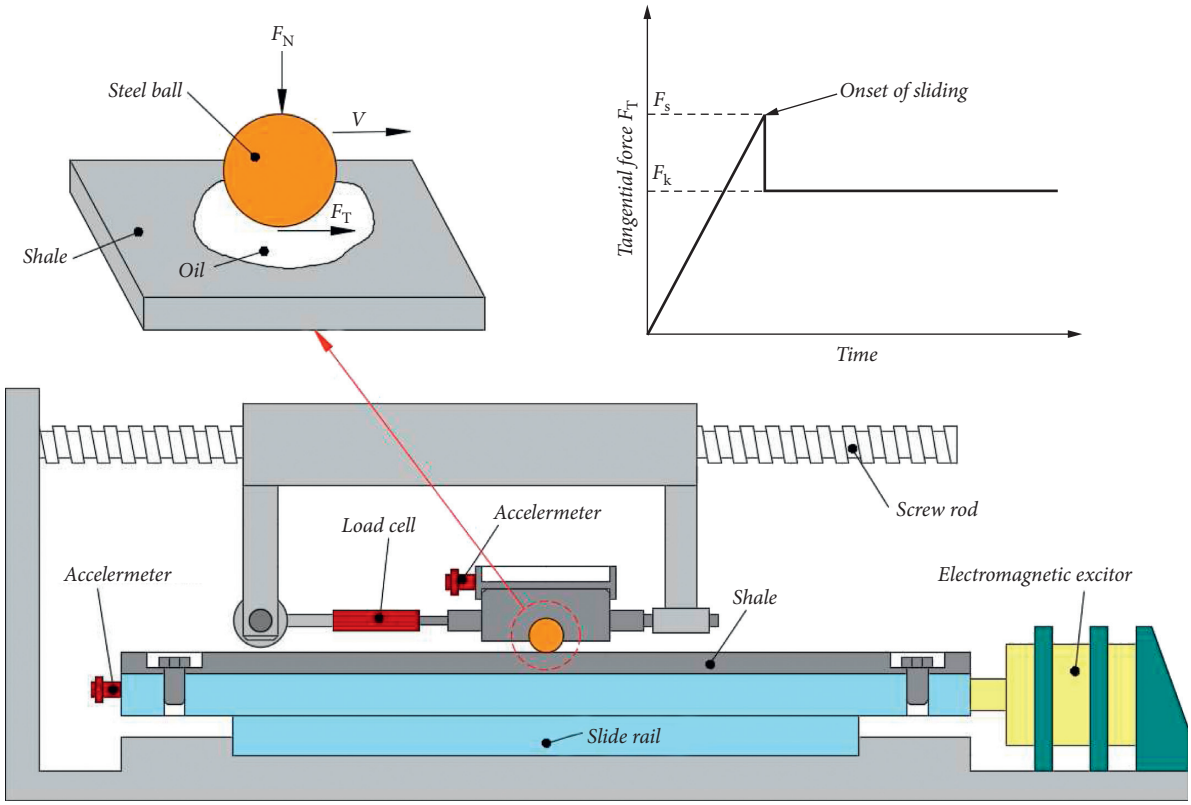

Figure 1: Experimental setup and a hypothetical static to kinetic friction transition diagram.

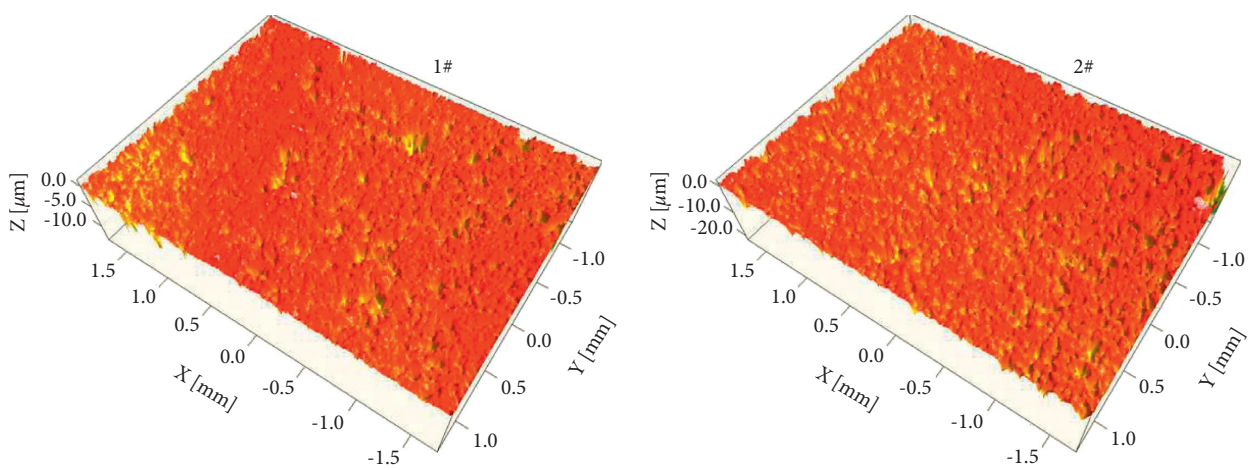

(a) (b)

Figure 2: Continued.

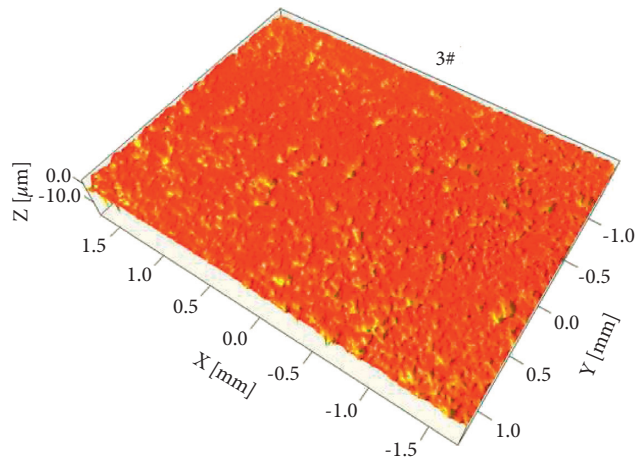

(c)

Figure 2: SEM micrographs of shale surfaces.

Table 1: Values of the surface morphology parameters of the shale specimen.

Roughness parameter (μm)	Shale 1#	Shale 2#	Shale 3#
R_a (arithmetic surface roughness value)	0.491	0.740	0.421
R_q (root-mean-square roughness)	0.693	0.944	0.622
R_k (core roughness depth)	1.011	1.667	0.970
R_{pk} (reduced peak height)	0.200	0.399	0.238
R_{vk} (reduced valley depth)	1.307	1.673	1.266

μm; R is the radius of curvature of asperities, $R = 8$ (when $R_a = 0.7$–0.8) or 12 (when $R_a = 0.4$–0.5), μm; E_1 and E_2 are Young's modulus of the steel ball and shale, respectively, MPa; and ν_1 and ν_2 are the Poisson ratio of the steel ball and shale, respectively.

The dot matrix nanoindentation method [42] was adopted to obtain the mechanical properties of the shale specimen, such as Young's modulus, hardness, and Poisson's ratio. The indenter gradually pressed into the shale specimen, the material near the pressure head first generated elastic deformation and changed to plastic deformation with the increase of load, and an indentation matching the shape of the indenter appeared in the sample. When the indenter was unloaded, the elastic deformation was restored, while the plastic deformation formed the indentation crack (see Figure 3). The load-displacement curve of the nanoindentation was drawn based on the experimental data, based on which Young's modulus and hardness of the shale were calculated. Substituting the surface morphology and mechanical parameters of steel/shale specimens measured into equations (1) and (2), the plasticity of the steel ball/shale pairs could be obtained, as shown in Table 2. From these values of the plasticity index, it can be concluded that both elastic and plastic deformations exist simultaneously.

3. Results

3.1. Friction Coefficient Change during Motion Restart. Figure 4 shows the change of frictional coefficient in the restarting process after 30 seconds of motionless. From Figures 4(a) and 4(b), the frictional coefficient first increases linearly to the maximum (i.e., the static friction) and then decreases exponentially to a steady value (i.e., the dynamic friction) with increasing sliding displacement in one sliding period under dry friction conditions, and the change laws of friction coefficient in the two sliding periods are almost the same, which means that the friction coefficient changes significantly in the transition process between motionless and sliding. From Figures 4(c) and 4(d), the static friction coefficient is significantly reduced, and there is no obvious transition between static and dynamic friction coefficients under lubricated conditions. The fluctuation of the frictional coefficient is due to the instability of the lubrication state between the contact surfaces.

3.2. Effect of Quiescent Time and Sliding Velocity. The effect of the quiescent time and sliding velocity on the transition from static to kinetic friction was studied under unlubricated and lubricated conditions. Figure 5 shows the effect of quiescent time on the friction coefficient measured on steel/shale under different normal loads and lubricating conditions. The static and kinetic friction coefficients were determined as the ratio of tangential force F_T at the peak and steady values divided by the applied normal load, respectively. When the steel ball began to slide, the tangential force increased almost linearly up to peak, and onset of the first slip was accompanied by a discontinuity in the course of F_T versus time. After the frictional coefficient reaches its maximum in the condition of dry friction, the frictional coefficient under higher normal load drops sharply to the kinetic friction coefficient, while this

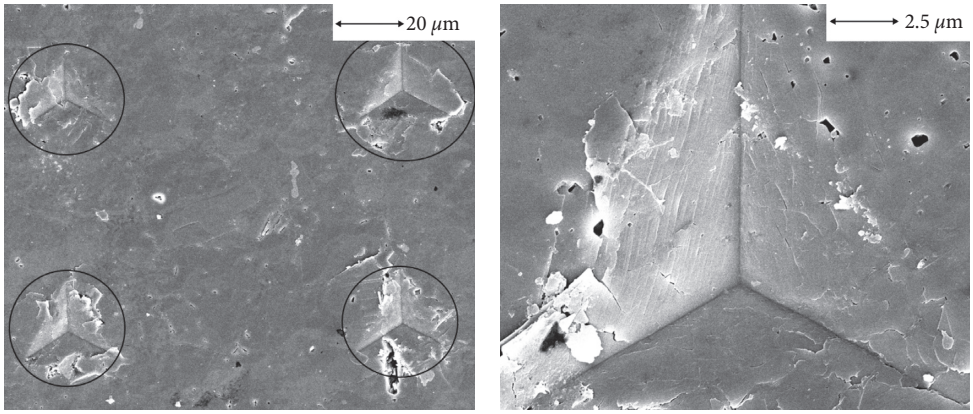

(a) (b)

Figure 3: SEM pictures of indentation. (a) Dot matrix. (b) Single.

Table 2: Mechanical parameters and plasticity index of steel/shale specimens.

Mechanical parameter	Steel ball	Shale 1#	Shale 2#	Shale 3#
E (GPa)	190		44.41	
ν	0.305		0.24	
(GPa)	1.0097		2.64	
R_q (μm)	0.28	0.693	0.944	0.622
R (μm)	20	12	8	12
ψ	4.51	3.50	5.00	3.32

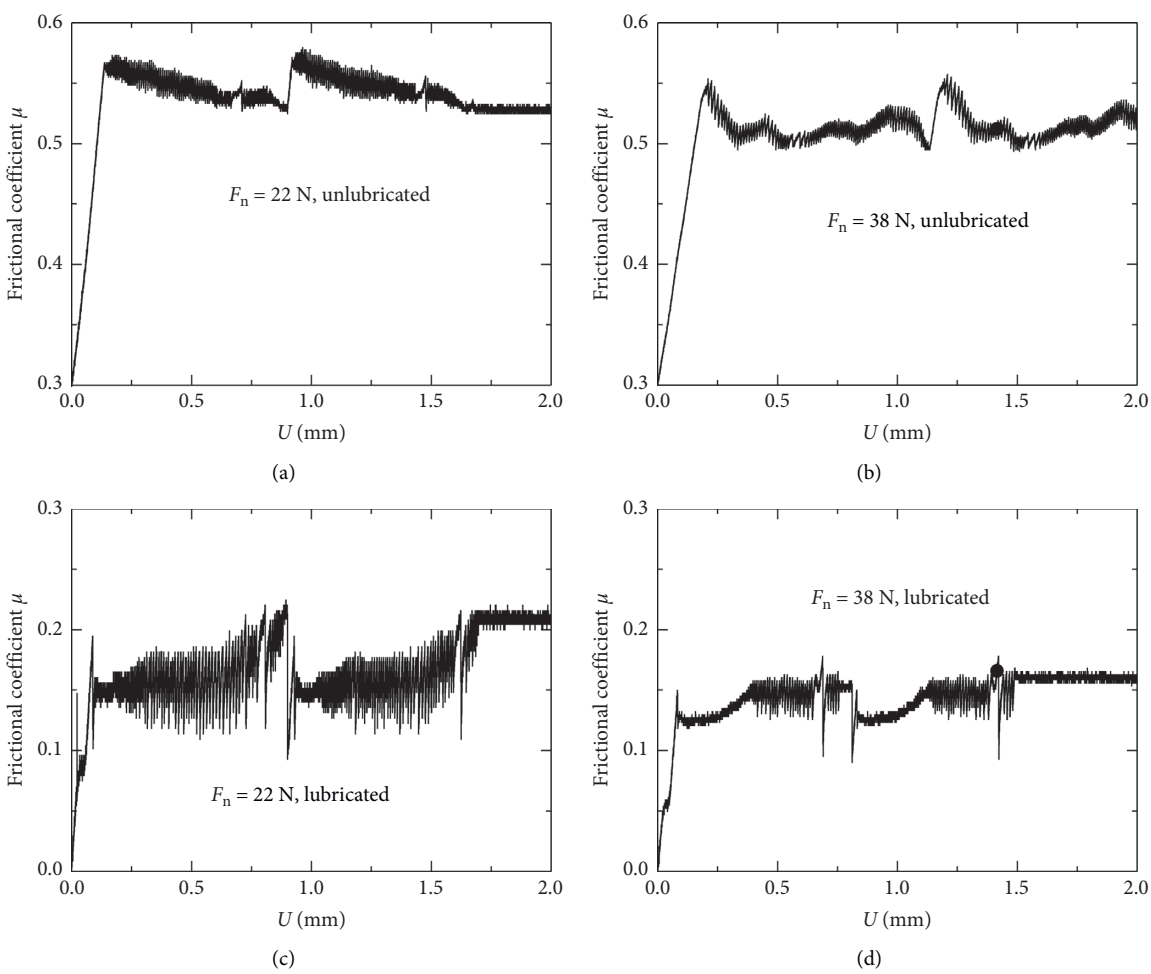

Figure 4: The friction coefficient during motion restart ($V = 22.78\,\mu m/s$ and quiescent time equals 30 s).

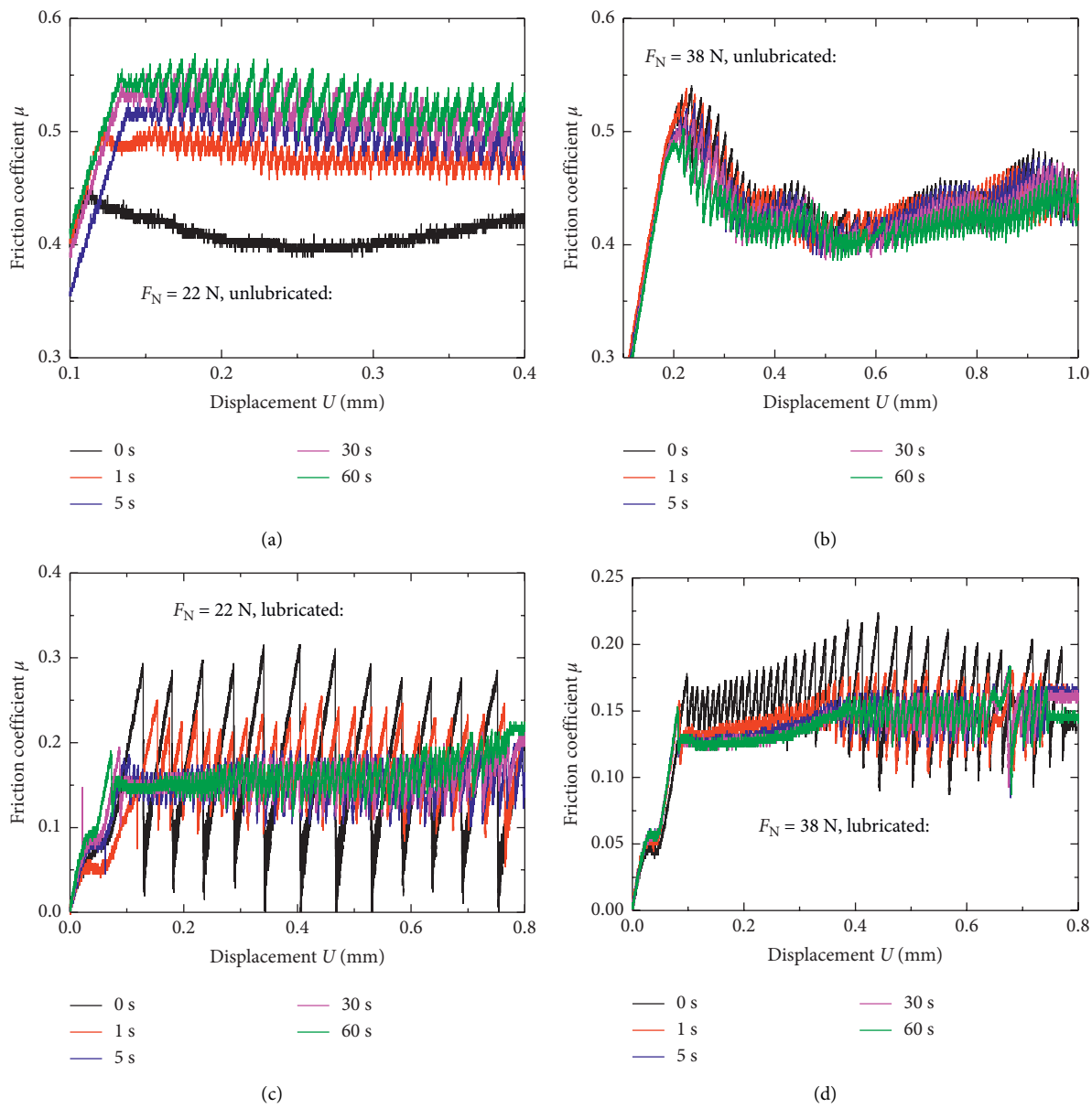

Figure 5: Effect of quiescent time on the transition from static to kinetic friction ($V = 22.78\mu m/s$).

process becomes very gentle under lower normal load. Under the lubricated condition, the average value of friction coefficient decreases significantly and fluctuates acutely compared with the unlubricated condition, and the boundary between static friction and dynamic friction becomes blurred. The quiescent time (from 0 to 60 s) between the adjacent sliding period had small effect on the average value of coefficient of friction for the unlubricated condition while larger effect for the lubricated condition. This may attribute to the influence of quiescent time on the distribution of lubricating oil. Larger quiescent time was beneficial to oil entering into the interface of rubbing pairs again where oil has been extruded in the preceding motion.

Figure 6 shows the effect of sliding velocity on the transition from static to kinetic friction under different normal loads. It can be seen that the average frictional coefficient increases (especially in higher normal load) with increasing sliding velocity, and the stick-slip motion intensifies which makes the transition between static and kinetic friction coefficients become indistinct. The main reason for the above phenomenon is that the higher sliding speed extrudes lubricating oil from the contact interface, resulting in an increase in the average friction coefficient. At the same time, the deterioration of lubrication conditions intensifies the stick-slip movement.

3.3. Transition from Static to Kinetic Friction. The following law was determined to model the transition from static to dynamic friction coefficient [12]:

$$\mu = \mu_d + (\mu_s - \mu_d)e^{-Cq}, \tag{3}$$

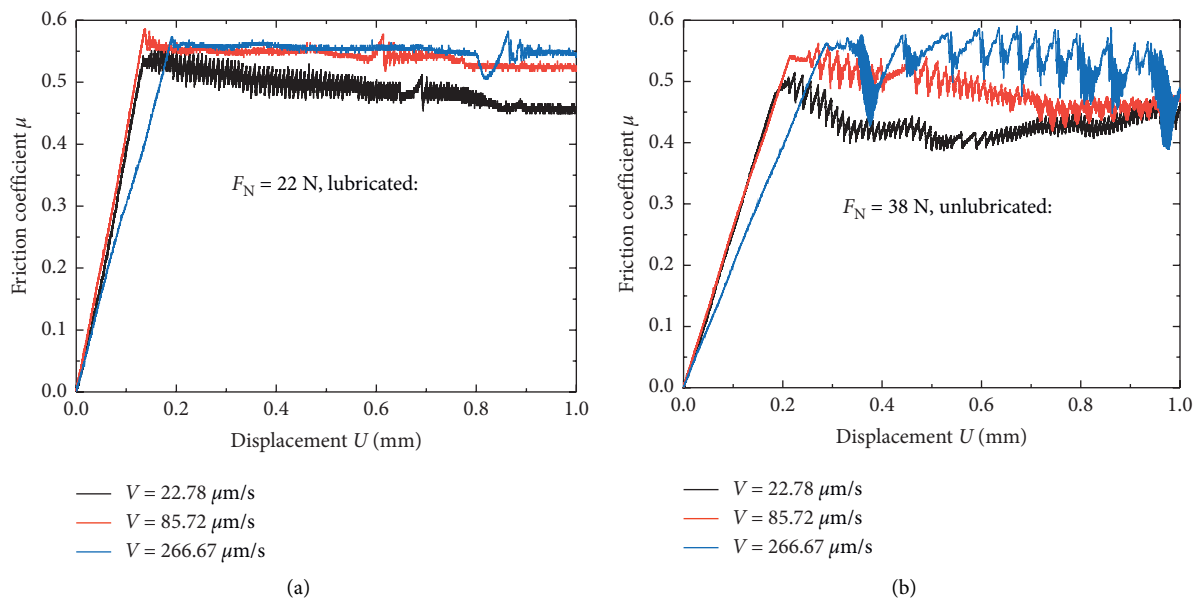

Figure 6: Effect of sliding velocity on the transition from static to kinetic friction.

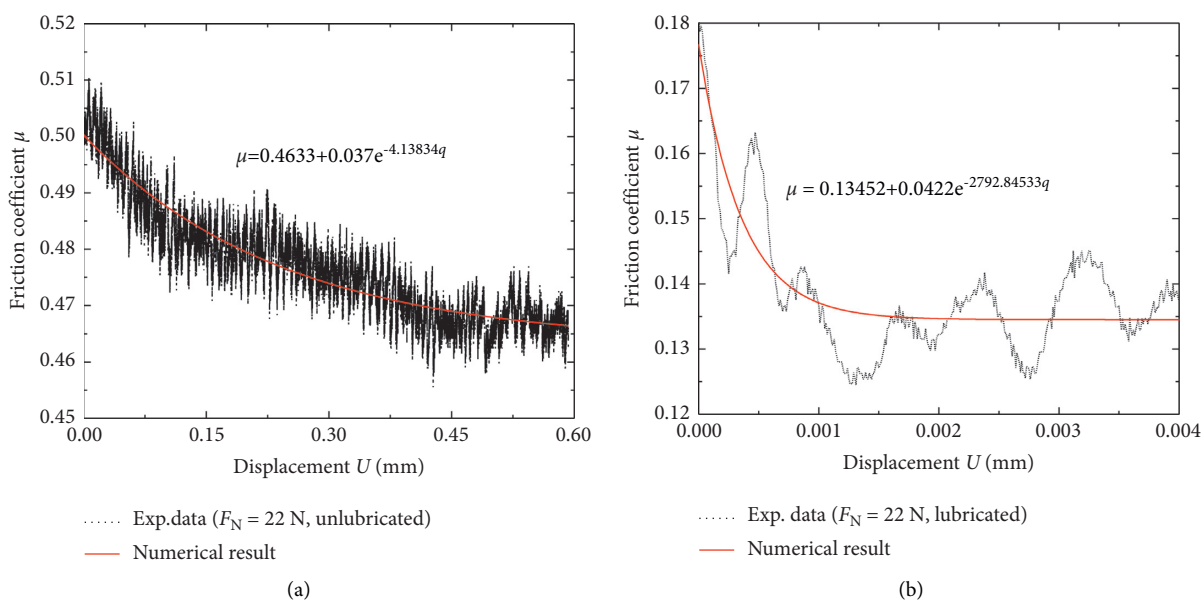

Figure 7: Continued.

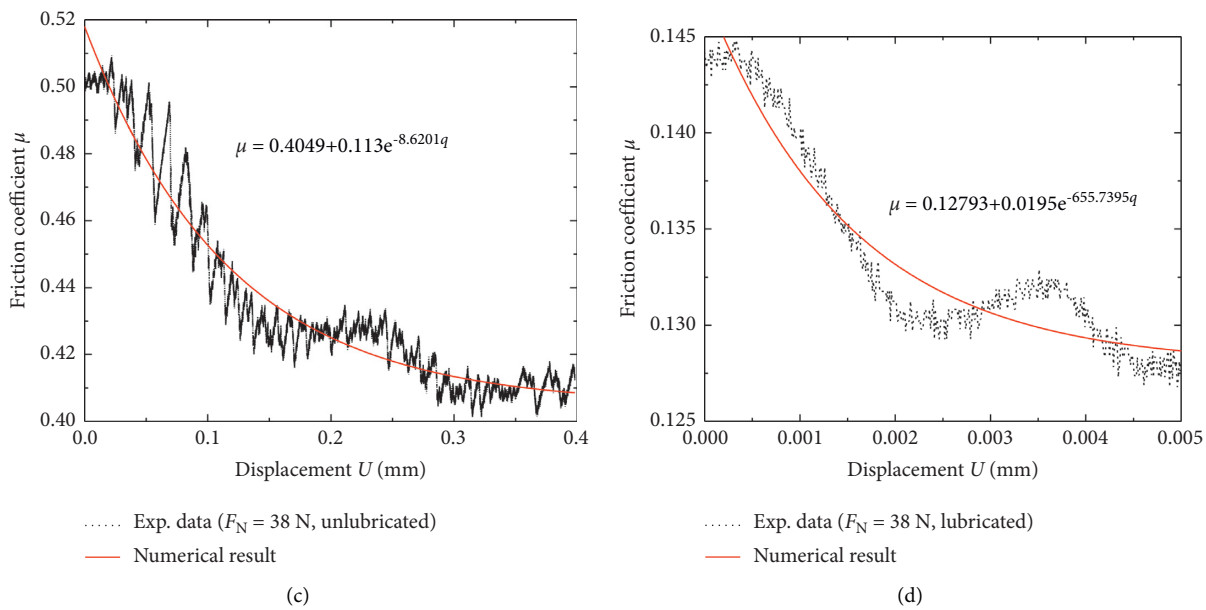

Figure 7: Fitting of the friction coefficient versus displacement ($V = 22.78\mu m/s$).

where q is the sliding distance, mm; C is a constant that determines the convergence rate; μ_d is the dynamic friction coefficient; and μ_s is the static friction coefficient.

Figure 7 shows the fitting results of the friction coefficient transition from static to kinetic friction using equation (3). It can be seen that the average friction coefficients decreased exponentially with increasing sliding displacement under both unlubricated and lubricated conditions. The difference between static and kinetic friction coefficients under the lubricated condition became smaller.

As the friction coefficients fluctuated sharply and depended on the quality of surfaces strongly under a higher sliding velocity, the experimental data of low sliding velocity ($V = 22.78\mu m/s$) in Figure 7 are chosen to analyze the critical distance D_c, which is the length to break the contact between asperities, leading to a continuous decrease of the friction coefficient until the kinetic value is reached. The calculated results of critical distance D_c for steel/shale pairs were compared with other materials [43], as shown in Figure 8. It can be seen that the critical distance D_c of steel/shale pairs under the lubricated condition is much smaller than that under the unlubricated condition and is close to the critical distance of metal materials while lower than the soft materials (such as acrylic or wood) (see Table 3). D_c decreases with increasing normal load under the dry friction condition, and D_c of the lubricated condition is much smaller than that of the dry friction condition, and the values of D_c are similar under different normal loads, which is consistent with the experimental results in the related literature [37].

4. Discussion

Normal load, quiescent time, sliding velocity, and lubrication influenced the static friction and transition from static to kinetic friction at the operating conditions used in this study. The static coefficient of friction of both unlubricated and lubricated pairs decreased with increasing normal load. The difference between static and dynamic coefficients increased with increasing normal load under the unlubricated condition, while its value changed little under the lubricated condition. The quiescent time influenced the friction coefficients a lot under low normal load while little under higher normal load. Under the condition of oil-free lubrication, the static friction coefficient increases with increasing sliding speed, and the transition from static to kinetic friction coefficients basically disappears.

Figure 9 shows the fiction coefficient measured under the unlubricated condition under the normal load of 38 N versus sliding displacement and the SEM micrographs of the friction track on the shale specimen. At the place of onset of first sliding, the friction force increased to the static friction coefficient (point 2, Figure 9(a)) owing to penetration of roughness peaks of the shale into the surface of the steel ball, and the surface showed white curve areas accordingly (Figure 9(b)) which revealed plastic deformation and shale broken, and several light white-banded scratches on the right of point 2 were also observed inside the friction track. When the tangential force overcomes the resistance to abrasive grooving of the steel surface and shear strength of shale (point 2), the static friction coefficient decreases to kinetic friction coefficient (point 3). From point 1 to point 3, the broken areas of the shale surface (white areas) increase first and then decrease and remain stable during subsequent sliding. The transition from the higher static to the lower kinetic friction coefficient with the steel/shale pair can be explained by the rupture of asperities of shale surfaces. Figure 10 shows the enlarged view of area between point 1 and point 2 with different magnification times shown in Figure 9(b); it can be seen that the area is low-lying, and a large number of broken mineral particles still attach to the

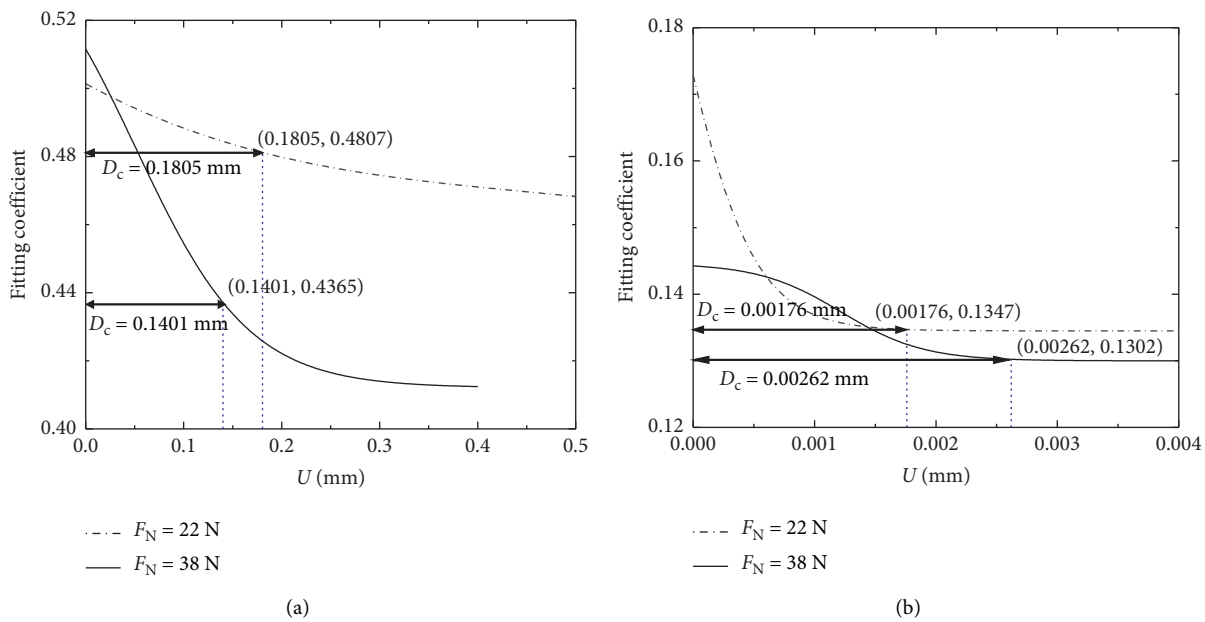

Figure 8: Average friction coefficient μ versus displacement U and the estimated D_c (V = 22.78μm/s). (a) Unlubricated. (b) Lubricated.

Table 3: Values of D_c for different materials [36, 38].

Materials	Un-/lubricated	μ_s	μ_k	D_c (μm)	Ref.
Mild steel on copper	Unlubricated	0.54	0.39	0.9	Rabinowicz, [35]
	Lubricated	0.58	0.40	0.7	
Mild steel on titanium	Unlubricated	0.63	0.45	6.0	
	Lubricated	0.61	0.45	5.0	
Acrylic on wood	Unlubricated	0.3	0.06	290.0	Mendez and Miguel [36]
Wood on wood	Unlubricated	0.2	0.07	420.0	
Steel on shale	Unlubricated	0.51	0.41	160.3	This paper
	Lubricated	0.144	0.13	2.19	

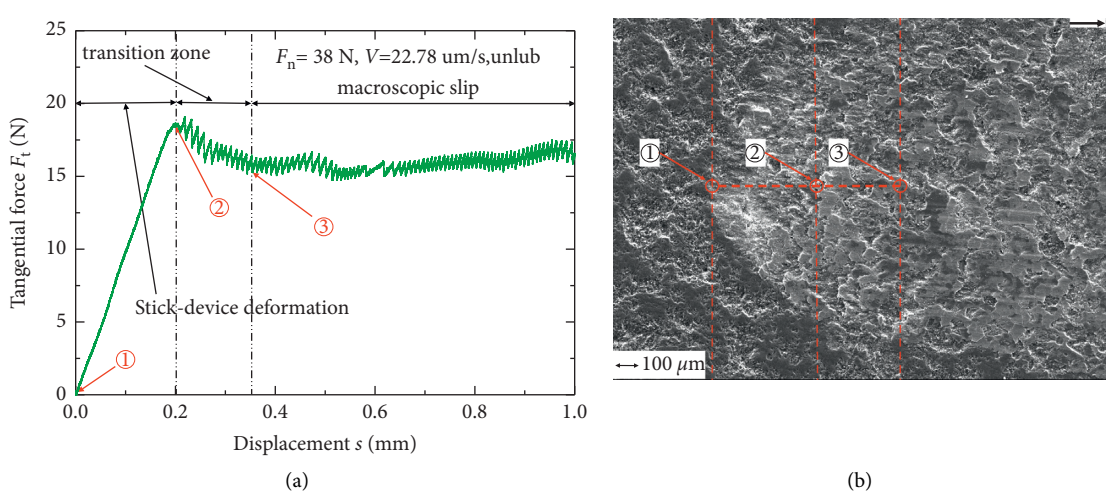

Figure 9: Tangential force measured on the unlubricated mild steel/shale pair versus time of testing. SEM micrographs of the contact area of the shale after different times of testing (arrows indicate the direction of tangential force applied).

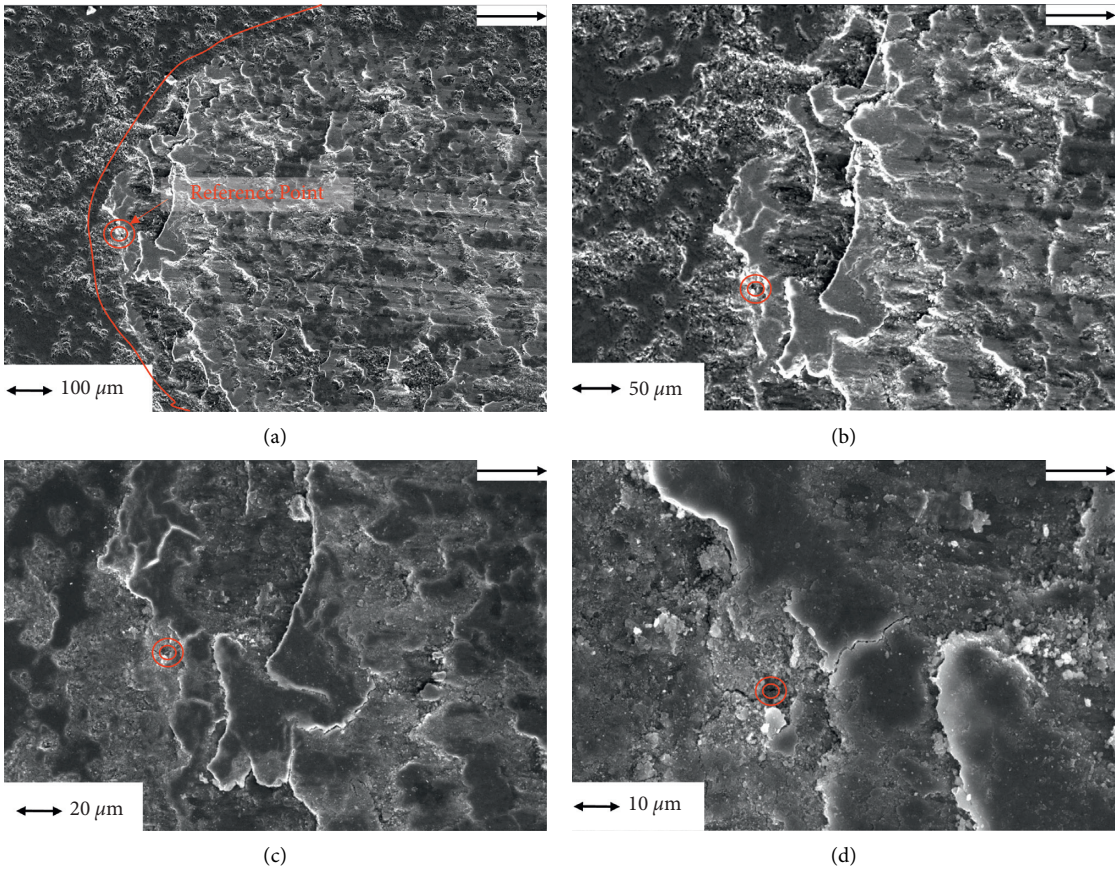

Figure 10: SEM micrographs of the shale surface at the area of first sliding (arrows show the direction of relative sliding). (a) ×100. (b) ×200. (c) ×300. (d) ×1000.

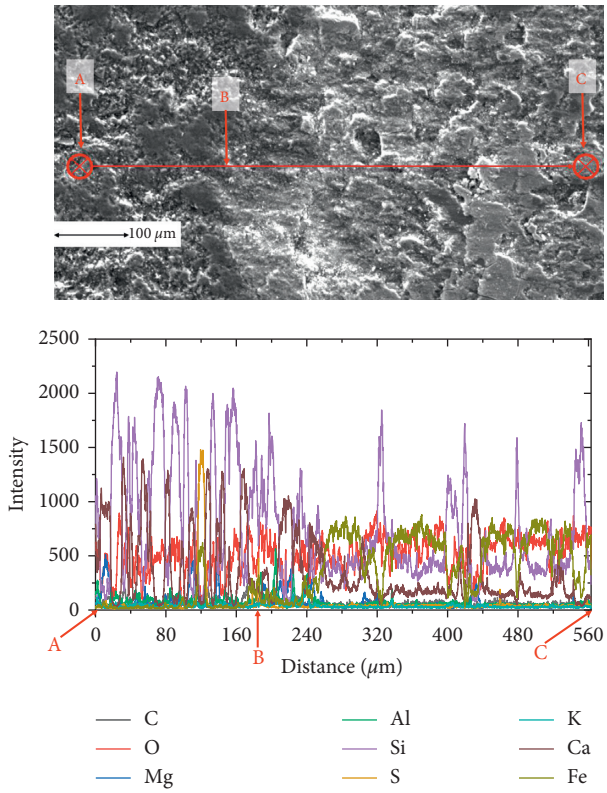

Figure 11: The material transfer between the steel ball and shale.

shale surface although the surface has been cleaned up before scanning.

Material transfer from the steel ball was detected on the contact surface of the shale specimen (Figure 11). Starting from the boundary of the scratch (point B), the proportion of Si and Ca elements decreases significantly, while that of the Fe element increases significantly. It indicates that the quartz minerals (Si element based), calcite, and dolomite (Ca element based) in the shale surface decrease after friction tests, which may be embedded in the steel ball surface or fractured and removed. At the same time, portion of the Fe element of the steel ball transfers to the shale surface. Transition behavior was changed, and kinetic friction of the steel/steel pairs was remarkably reduced by oil lubrication in this paper. Stick-slip effects (Figures 5(c) and 5(d)) occurred on the lubricated steel/shale pairs. This was attributed to squeezing out of oil from the contact area with the onset of sliding and hence increasing asperities' contact on the mated surfaces. The friction coefficient increases until the resistance to stick owing to grooving, asperity interlocking, and/or adhesive junctions, as well as material transfer is overcome, and slip occurs.

5. Conclusions

The results of the experimental investigation demonstrate that the coefficient of friction of steel/shale pairs decreases exponentially from static to dynamic friction coefficient with increasing sliding displacement. The difference between static and dynamic friction coefficients and the critical distance D_c under the dry friction condition is much larger than that under the lubricated condition. The transition from static to dynamic friction coefficient is greatly affected by the normal load, quiescent time, and sliding velocity, especially the lubricating condition. Maintaining continuous lubrication of the contact area by the lubricant is crucial to reduce or eliminate the stick-slip motion. Static and kinetic frictions are determined by destroying the surface natural oxide film of steel and the skin layer asperities of shale, microgrooving owing to protruding carbides of the steel and mineral of the shale forming or breaking, respectively, of adhesive junctions. The change laws of friction of stick-slip motion between steel and shale and the empirical formula of friction coefficient fitting from the experimental data in this study provide an insight into the transition from static to dynamic friction of steel/shale pairs and have tremendous guiding significance in the accurate value of friction force between the drill string and borehole wall under the sliding drilling condition, which is the key to realize intelligent drilling.

Data Availability

The data used to support the findings of this study are available within the article.

Conflicts of Interest

The authors declare that they have no conflicts of interest.

Acknowledgments

The authors gratefully acknowledge the financial support of the Major Science and Technology Innovation Project of Shandong Province (Grant no. 2019JZZY010446) and the Fundamental Research Funds for the Central Universities (Grant no. 20CX02322A).

References

[1] C. Gillan, S. G. Boone, M. G. Leblanc, R. P. Picard, and R. T. Fox, "Applying computer based precision drill pipe rotation and oscillation to automate slide drilling steering control," in *Proceedings of the Canadian Unconventional Resources Conference*, p. 11, 2011.

[2] N. R. Zwarich, A. R. McSpadden, M. A. Goodman, R. Trevisan, and R. F. Mitchell, "Application of a new dynamic tubular stress model with friction," in *Proceedings of the IADC/SPE Drilling Conference and Exhibition*, p. 19, 2018.

[3] M. Abughaban, A. Alshaarawi, C. Meng, G. Ji, and W. Guo, "Optimization of drilling performance based on an intelligent drilling advisory system," in *Proceedings of the International Petroleum Technology Conference*, p. 17, Beijing, China, 2019.

[4] N. D. J. P. T. Spencer, "Sliding friction: physical principles and applications," *Physics Today*, vol. 52, pp. 66–68, 1999.

[5] H. Olsson and K. J. Astrom, "Friction generated limit cycles," *IEEE Transactions on Control Systems Technology*, vol. 9, no. 4, pp. 629–636, 2001.

[6] E. J. Berger and T. J. Mackin, "On the walking stick-slip problem," *Tribology International*, vol. 75, pp. 51–60, 2014.

[7] P. E. Rossouw, L. S. Kamelchuk, and R. P. Kusy, "A fundamental review of variables associated with low velocity frictional dynamics," *Seminars in Orthodontics*, vol. 9, no. 4, pp. 223–235, 2003.

[8] K. Nakano, "Two dimensionless parameters controlling the occurrence of stick-slip motion in a 1-DOF system with Coulomb friction," *Tribology Letters*, vol. 24, no. 2, pp. 91–98, 2006.

[9] K. Nakano and S. Maegawa, "Stick-slip in sliding systems with tangential contact compliance," *Tribology International*, vol. 42, no. 11-12, pp. 1771–1780, 2009.

[10] C. A. Brockley and H. R. Davis, "The time-dependence of static friction," *Journal of Tribology*, vol. 12, pp. 35–41, 1968.

[11] J. E. Dunkin and D. E. Kim, "Measurement of static friction coefficient between flat surfaces," *Wear*, vol. 193, no. 2, pp. 186–192, 1996.

[12] J. F. Ferrero and J. J. Barrau, "Study of dry friction under small displacements and near-zero sliding velocity," *Wear*, vol. 209, no. 1-2, pp. 322–327, 1997.

[13] T. Baumberger, P. Berthoud, and C. Caroli, "Physical analysis of the state- and rate-dependent friction law. II. Dynamic friction," *Physical Review B*, vol. 60, no. 6, pp. 3928–3939, 1999.

[14] M. Eriten, A. A. Polycarpou, and L. A. Bergman, "A physics-based friction model and integration to a simple dynamical system," *Journal of Vibration and Acoustics*, vol. 134, 2012.

[15] M. Eriten, "Multiscale physics-based modeling of friction," *Dissertations & Theses Gradworks.*, 2012.

[16] M. Eriten, A. A. Polycarpou, and L. A. Bergman, "Physics-based modeling for fretting behavior of nominally flat rough surfaces," *International Journal of Solids and Structures*, vol. 48, no. 10, pp. 1436–1450, 2011.

[17] B. Bhushan, "Contact mechanics of rough surfaces in tribology: multiple asperity contact," *Tribology Letters*, vol. 4, pp. 1–35, 1998.

[18] U. Andreaus and P. Casini, "Dynamics OF friction oscillators excited BY a moving base and/or driving force," *Journal of Sound and Vibration*, vol. 245, no. 4, pp. 685–699, 2001.

[19] J. Awrejcewicz and P. Olejnik, "Analysis of dynamic systems with various friction laws," *Applied Mechanics Reviews*, vol. 58, no. 6, pp. 389–411, 2005.

[20] J. Swevers, F. Al-Bender, C. G. Ganseman, and T. Projogo, "An integrated friction model structure with improved presliding behavior for accurate friction compensation," *IEEE Transactions on Automatic Control*, vol. 45, no. 4, pp. 675–686, 2000.

[21] W. Jerzy, S. Andrzej, W. Marian, T. Kapitaniak, and A. Stefa Ski, "Hysteretic effects of dry friction: modelling and experimental studies," *Philosophical Transactions of the Royal Society A Mathematical Physical & Engineering Sciences*, vol. 366, pp. 747–765, 2008.

[22] A. Ruina, "Slip instability and state variable friction laws," *Journal of Geophysical Research: Solid Earth*, vol. 88, no. B12, pp. 10359–10370, 1983.

[23] C. Canudas de Wit, H. Olsson, K. J. Astrom, and P. Lischinsky, "A new model for control of systems with friction," *IEEE Transactions on Automatic Control*, vol. 40, no. 3, pp. 419–425, 1995.

[24] P. Dupont, V. Hayward, B. Armstrong, and F. Altpeter, "Single state elastoplastic friction models," *IEEE Transactions on Automatic Control*, vol. 47, no. 5, pp. 787–792, 2002.

[25] P. Dahl, *A Solid Friction Model*, p. 31, Aerospace Cooperation, El Segundo, CA, USA, 1968.

[26] J. H. Dieterich, "Time-Dependent friction in rocks," *Journal of Geophysical Research*, vol. 77, no. 20, pp. 3690–3697, 1972.

[27] J. H. Dieterich, "Modeling of rock friction: 2. Simulation of preseismic slip," *Journal of Geophysical Research*, vol. 84, no. B5, pp. 2169–2175, 1979.

[28] J. H. Dieterich, "Time-dependent friction and the mechanics of stick-slip," *Pure and Applied Geophysics PAGEOPH*, vol. 116, no. 4-5, pp. 790–806, 1978.

[29] N. M. Beeler, T. Tullis, and J. D. Weeks, "The roles of time and displacement in the evolution effect in rock friction," *Geophysical Research Letters*, vol. 21, 1994.

[30] T. Baumberger and C. Hiver, "Physical analysis of the state- and rate-dependent friction law: static friction," *Physical Review B: Condensed Matter*, vol. 59, 1999.

[31] J. Rice and A. Ruina, "Stability of steady frictional slipping," *Journal of Applied Mechanics-transactions of The Asme - J APPL MECH*.vol. 50, 1983.

[32] W. Xueying, H. Ni, R. Wang, L. Zhang, and P. Wang, "Drag-reduction and resonance problems of a jointed drillstring in the presence of an axial excitation tool," *Journal of Energy Resources Technology*, vol. 141, Article ID 032904, 2019.

[33] P. Wang, H. Ni, W. Xueying, and R. Wang, "Modelling the load transfer and tool surface for friction reduction drilling by vibrating drill-string," *Journal of Petroleum Science and Engineering*, vol. 164, 2018.

[34] M. Sarker, D. G. Rideout, and S. D. Butt, "Dynamic model for longitudinal and torsional motions of a horizontal oilwell drillstring with wellbore stick-slip friction," *Journal of Petroleum Science and Engineering*, vol. 150, pp. 272–287, 2017.

[35] E. Rabinowicz, "The nature of the static and kinetic coefficients of friction," *Journal of Applied Physics*, vol. 22, no. 11, pp. 1373–1379, 1951.

[36] B. Mendez and R. Miguel, "Transition from the static to the kinetic coefficient of friction," 2020.

[37] E. K. Mitchell, Y. Fialko, and K. M. J. G. G. G. Brown, "Frictional properties of gabbro at conditions corresponding to slow slip events in subduction zones," *Geochemistry Geophysics Geosystems*, vol. 16, 2015.

[38] K. Tian, Z. Li, N. N. Gosvami, D. L. Goldsby, and R. W. C. J. A. Nano, "The memory distance for interfacial chemical bond-induced friction at the nanoscale," vol. 13, 2019.

[39] Q. Li, T. E. Tullis, D. Goldsby, and R. W. Carpick, "Frictional ageing from interfacial bonding and the origins of rate and state friction," *Nature*, vol. 480, no. 7376, pp. 233–236, 2011.

[40] P. Wang, H. Ni, R. Wang, Z. Li, and Y. Wang, "Experimental investigation of the effect of in-plane vibrations on friction for different materials," *Tribology International*, vol. 99, pp. 237–247, 2016.

[41] D. J. Whitehouse, "Surface topography and quality and its relevance to wear," in *proceedings of the Fundamentals of Tribology*, pp. 17–52, Massachusetts Institute of Technology, Cambridge, MA, USA, 1978.

[42] X. Shi, S. Jiang, S. Lu et al., "Investigation of mechanical properties of bedded shale by nanoindentation tests: a case study on Lower Silurian Longmaxi Formation of Youyang area in southeast Chongqing, China," *Petroleum Exploration and Development*, vol. 46, no. 1, pp. 163–172, 2019.

[43] K. Jankowski, A. Saha, and A. Stefański, "Introduction of novel model of friction and analysis of presliding domain of friction with non-local memory effect based upon Maxwell slip model structures," *Tribology International*, vol. 102, pp. 378–391, 2016.

Hindawi
Shock and Vibration
Volume 2021, Article ID 5089213, 16 pages
https://doi.org/10.1155/2021/5089213

Research Article

Design and Investigation of a Nonlinear Damper Based on Energy Dissipation through Shock and Dry Friction to Suppress Critical Self-Excited Vibrations in Drilling Systems

Vincent Kulke,[1] **Georg-Peter Ostermeyer**,[1] **and Andreas Hohl**[2]

[1]*TU Braunschweig, Institute of Dynamics and Vibrations, Braunschweig 38106, Germany*
[2]*Baker Hughes, Celle 29221, Germany*

Correspondence should be addressed to Georg-Peter Ostermeyer; gp.ostermeyer@tu-bs.de

Received 26 July 2021; Accepted 31 August 2021; Published 26 September 2021

Academic Editor: Peng Wang

In this paper, a passive damper based on energy dissipation through shock and dry friction (shock-friction damper) is investigated regarding its design and effectiveness for damping self-excited torsional vibrations similar to those occurring in deep drilling. The results are compared to the results of conventional friction dampers. The effectiveness of the damper for different operational drilling parameters that change during the drilling process, such as the weight on the bit and the rotary speed of the bit, is analyzed. Two linear reduced order models of a drill string that are based on a complex finite element model are set up. One is reduced using the component mode synthesis and one is reduced to the identified critical mode. A lumped mass represents the inertia of a forcedly connected nonlinear damper. A combined reduced order model of the complex system and the inertia damper is introduced to investigate its dynamic motion and stability. Particular focus is on the energy flow within the dynamic system and on the change of the dissipation energy in the contact. A semi-analytical solution is derived using the harmonic balance method that is used to investigate the damping effect for various designs and operational parameters. Herein, the modal properties as well as parameters of the damper are examined regarding the damping effect and the stability of the system. Finally, the capability of the mechanism to suppress the self-excitation due to the bit–rock interaction in a drilling system is discussed, and recommendations are made with respect to the design parameters and placement of the damper.

1. Introduction

In downhole drilling systems, various types of vibrations occur that can reduce drilling performance and reliability as well as increase premature failure of components and nonproductive time [1, 2]. Especially when drilling in hard and dense formations, high-frequency torsional oscillations (HFTO) occur [3] in a system-dependent frequency range between 50 Hz and 500 Hz. These oscillations are self-excited torsional vibrations of higher-order modes that are caused by the bit-rock interaction [4] and that can lead to critical torsional loads [1, 5]. Downhole measurement data show that in most cases one high-frequency torsional mode dominates the dynamic of the drilling system [6, 7]. The self-excitation mechanism, which leads to the critical torsional loads, can be modeled by a torque characteristic at the bit that is nonlinear with respect to the rotary speed (Figure 1) [8].

In [8], an analytical predictive criterion

$$S_{c,i} = \frac{-2D_i\omega_{0,i}}{\varphi_{i,\mathrm{bit}}^2} < \frac{d\mathrm{Torque}}{d\mathrm{RPM}}, \tag{1}$$

based on a modal transformation (modal damping constant D_i, natural angular frequency $\omega_{0,i}$, and deflection of the mass-normalized eigenvector of mode i at the bit $\varphi_{i,\mathrm{bit}}$) and linearization of the nonlinear torque characteristic at the bit (dTorque/dRPM) are introduced. This $S_{c,i}$ criterion is used to determine modes that are unstable and thus prone to self-excitation. Additionally, based on the observation that no backward rotation of the bit can occur [4], a criterion for the worst-case amplitude $\hat{x} = (2\pi/(60\mathrm{sec/min}))\mathrm{RPM}\,(1/\omega_{0,i})$ of

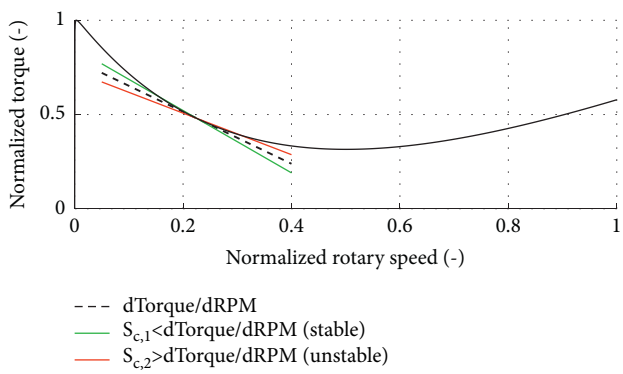

Figure 1: Nonlinear torque characteristic with lines at the operating point c.f. [9, 10].

these critical modes is derived [9]. The worst-case amplitude is a reliable criterion when one mode dominates the dynamic of the system, but also delivers good results if an interaction between low-frequency stick/slip and HFTO is observed [6]. In [10], this interaction is analyzed using downhole measurement data and simulations of a modal reduced order model representing the torsional mode of stick/slip and HFTO. The bit–rock interaction is modeled as a nonlinear drilling torque characteristic as a function of the rotary speed and weight on bit (WOB) similar to Figure 1. Through the resulting stability maps, suitable drilling conditions are determined by adjusting operational parameters such as rotary speed or WOB to reduce critical drill string vibrations based on the overlap of the stability maps of stick/slip and HFTO. Besides reducing the WOB that results in a smaller negative slope of the torque characteristic, an increase of the rotary speed can stabilize the system due to an increasing torque characteristic at high rotary speeds (Figure 1). Furthermore, the stable areas in the stability maps can be extended by adding damping to the system [11–13]. Since the drilling parameters cannot be adjusted arbitrarily, further concepts have to be investigated. In downhole drilling systems, concepts based on isolation [14], energy transfer [15], and additional damping [12, 13] have been discussed in the literature.

Additional tools that are placed within the drill string have been investigated to reduce critical torsional vibration. In [14], an isolator tool is investigated in simulation, laboratory tests, and operation. This tool, which is based on the principle of a mechanical low-pass filter, can isolate critical areas of the bottom-hole assembly (BHA) from torsional vibrations induced by the bit–rock interaction. Increasing the damping of a system is another well-known approach to reduce self-excited vibration amplitudes [16]. Tondl investigated the effect of tuned mass dampers [17] and dry friction [18] on self-excited vibrations. Some types of friction contacts and friction dampers for various fields of engineering were investigated and classified [19]. Examples for vibration reduction through friction damping are found in the field of gas turbines [20], mounted structures [19], and railway wheels [21, 22]. In the field of drilling systems, the effectiveness of inertia-based and stiffness-based dampers are analyzed in [12], and a nonlinear tuned damper is analyzed in [13]. Due to the small design space in the BHA that is naturally limited by the drilled borehole diameter, the additional damping provided by the damper is limited and possibly not sufficient to stabilize unstable self-excited vibrations.

Similar efforts for nonlinear attachments show a significant effect on the energy output and stability of dynamic systems [23, 24]. While the damping effect of friction is directly related to the dissipation processes in the contact, the energy transfer caused by shocks can have various effects on the dynamic motion and energy balance of the system. Shocks can add energy to a system, dissipate energy from the system, and redistribute energy within the system. In [25], shocks are used to suppress self-excited vibrations through energy transfer from low- to high-frequency modes, which results in an increased damping ratio. Another possibility to use shocks to reduce vibrations are various types of impact dampers. These dampers range from simple lumped masses coupled to a structure by a mechanical backlash [26, 27] up to self-tuning impact vibration dampers [28]. In general, an impact damper causes shocks as soon as a clearance width is exceeded. Due to the collision between the impact damper and a structure, energy is dissipated and momentum is exchanged between the impact damper and the structure. Various impact dampers have already been analyzed analytically [29] as well as in simulations and experiments [30].

The challenges in drill string dynamic and the possibility of influencing the energy balance and, if applicable, the damping effect through shocks necessitates further investigation. Optimization of these highly nonlinear damping concepts to increase the provided damping for critical torsional modes, hence stabilize the self-excited modes, is important. In the following article, a friction damper comparable to [12, 21] is combined with an impact damper through an additional mechanical backlash that results in shocks between the structure and the damper [31, 32]. The resulting shocks can increase the damping effect through energy transfer from the self-excited structure to the damper and thus increase the dissipated energy in the friction contact. The increase in damping is evaluated qualitatively and quantitatively, and the influences of critical parameters are investigated regarding the stability of self-excited drill string modes. A semi-analytical and an analytical solution for the design of the damper is derived by using the harmonic balance method. The semi-analytical solutions are compared to time domain simulations of an entire self-excited drilling system.

2. Modelling a Passive Shock-Friction Damper in a Drilling System

To investigate drill string vibrations, a finite element model of an entire drill string (Figure 2) with the vector of angular deviations x from the operating point (for a constant angular speed and twist) with $\mathbf{M}\ddot{\mathbf{x}} + \mathbf{C}\dot{\mathbf{x}} + \mathbf{K}\mathbf{x} = \mathbf{f}$ is used. Herein, $\mathbf{M}, \mathbf{C}$, and $\mathbf{K}$ are the mass, damping, and stiffness matrices, and $\mathbf{f}$ is an external force vector.

To perform an efficient and accurate investigation of the dynamic motion of various additional dampers like the

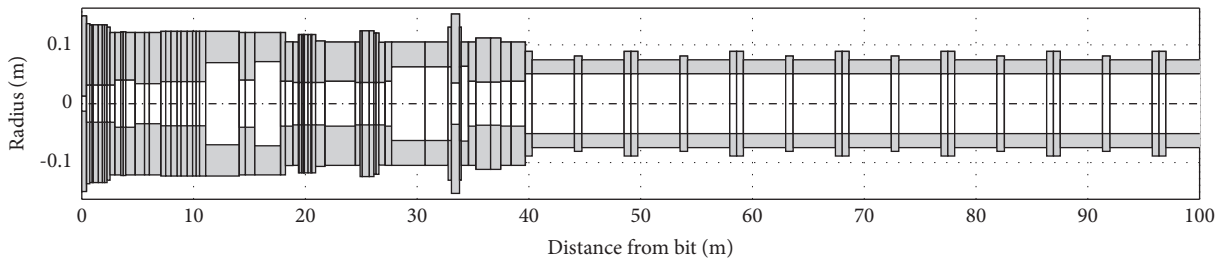

Figure 2: Model of a generic drill string.

nonlinear shock-friction damper, a reduced order model of the complex finite element model of the drilling system is derived.

In the following section, two reduction methods are carried out. First, the system is reduced using the component mode synthesis (CMS or Craig-Bampton method) resulting in a multiple-degree-of-freedom system with modal and physical degree-of-freedom [33, 34]. Second, the system is modally reduced to a modal single-degree-of-freedom system, representing the most critical and therefore dominant mode of the system [8, 12, 13]. Finally, a nonlinear damper is added to the different linear models of the drilling system. In both cases, the shock-friction damper is forcedly connected to the structure at one specific point of the BHA.

2.1. Component Mode Synthesis. The component mode synthesis is a reduction method based on a static and modal reduction, that is, specifically useful in systems with strong local nonlinearities to reduce the linear components [34]. All nodes u are divided into master u_{M} and slave u_{S} nodes and are rearranged regarding the mass M and stiffness matrix K according to

$$\begin{bmatrix} M_{\mathrm{SS}} & M_{\mathrm{SM}} \\ M_{\mathrm{MS}} & M_{\mathrm{MM}} \end{bmatrix} \begin{pmatrix} \ddot{u}_{\mathrm{S}} \\ \ddot{u}_{\mathrm{M}} \end{pmatrix} + \begin{bmatrix} K_{\mathrm{SS}} & K_{\mathrm{SM}} \\ K_{\mathrm{MS}} & K_{\mathrm{MM}} \end{bmatrix} \begin{pmatrix} u_{\mathrm{S}} \\ u_{\mathrm{M}} \end{pmatrix} = \begin{pmatrix} 0 \\ p_M \end{pmatrix}. \tag{2}$$

The master nodes are kept as physical coordinates where nonlinear forces act, while the slave nodes are modally reduced to so-called fixed interface modes. First, the static transformation matrix T_{stat} is determined $u_{\mathrm{S}} = K_{\mathrm{SS}}^{-1} K_{\mathrm{SM}} u_{\mathrm{M}} = T_{\mathrm{stat}} u_{\mathrm{M}}$. Second, the dynamic transformation matrix T_{dyn} is determined by a modal transformation of the slave nodes (with fixed master nodes) through $M_{\mathrm{SS}} \ddot{u}_{\mathrm{S}} + K_{\mathrm{SS}} u_{\mathrm{S}} = 0$, resulting in the transformation matrix T.

$$T = \begin{bmatrix} T_{\mathrm{dyn}} & T_{\mathrm{stat}} \\ 0 & E \end{bmatrix}, \tag{3}$$

with the uniform matrix E. The new transformed mass M_{T} and stiffness matrix K_{T} are calculated using

$$\begin{aligned} M_{\mathrm{T}} &= T^T M T, \\ K_{\mathrm{T}} &= T^T K T. \end{aligned} \tag{4}$$

The system is reduced by consideration of only a subset of modes in the modal transformation matrix, hence reducing the number of fixed interface modes [33] (rank of the matrix). As a thumb rule, all fixed interface modes with frequencies smaller than three times the characteristic frequency should be considered [35]. A convergence analysis has shown similar results in drill string dynamics. The CMS model used here has three master nodes, one master node at the bit $u_{\mathrm{M,bit}}$ (lowest node of the BHA model), where the nonlinear forces from the bit–rock interaction occur (Figure 1), one master node at the top drive $u_{\mathrm{M,top}}$ (highest node of the BHA model), where the constant rotary speed is applied and one master node $u_{\mathrm{M,d}}$ where the damper is connected to the BHA. The first two master nodes can be neglected when linearizing the motion of the BHA with respect to the operating point (average rotary speed and average torque at the bit).

The bit-rock interaction is modeled by a torque characteristic that is nonlinear with respect to the relative velocity between the bit and the rock (Figure 1). If the system is linearized to a specific operational rotary speed, the nonlinear torque characteristic with a negative/positive slope is equivalent to a negative/positive modal damping ratio [8]. Therefore, the self-excitation mechanism in the operational parameters can be modeled by a negative modal damping of the critical mode or modes.

2.2. Modal Reduction. Downhole measurement data show that in most cases when HFTO occur, one critical mode dominates the dynamic motion of the entire drill string [6, 7]. In this case, the dynamic motion of the entire drill string can be modeled by a modal single-degree-of-freedom system:

$$\ddot{q} + 2D_i \omega_{0,i} \dot{q} + \omega_{0,i}^2 q = \sum_{j=1}^{n} \varphi_{i,j} M_j, \tag{5}$$

where $\omega_{0,i}$ and D_i are the natural frequency and modal damping ratio of the ith mode q ($D_i < 0$ for self-excited modes). M_j is an external torque that acts on the jth node, and $\varphi_{i,j}$ is the mass-normalized modal amplitude of the ith mode shape at the jth node. In [8], a predictive criterion is derived through modal transformation and linearization of the rotary speed-dependent friction characteristic at the bit, resulting in $S_{\mathrm{c},i} = -2D_i \omega_{0,i} / \varphi_{i,\mathrm{bit}}^2$ for every mode. The self-excitation occurs due to the bit–rock interaction, hence $\varphi_{i,\mathrm{bit}}$ is the mass-normalized modal amplitude at the bit. Using this criterion, the dominant (most critical) mode is determined. This mode is considered as the ith and only mode in the minimal model.

2.3. Additional Friction-Based Damper. Any nonlinear torque can act at the master node $u_{\mathrm{M,d}}$ of the CMS reduced model or at any node (e.g., the jth node) of the minimal model with a mass-normalized amplitude of the mode shape $\varphi_{i,j}$. The added damper (Figure 3 (red)) consists of an inertia ring with a rotational inertia J. The torque between the inertia ring (Figure 3 (red)) and the structure (Figure 3 (blue)) consists of a friction contact with a normal force F_{N}, a coefficient of friction μ, and a friction radius r as well as a mechanical backlash with a contact stiffness c, damping constant d, an angular backlash width β_{S}, and a linearity constant e which models a linear stiffness and damping value for $e = 1$ and a nonlinear stiffness or damping value for $e \neq 1$ (e.g., Hertzian stiffness $e = 3/2$).

$$M\left(x_{\mathrm{rel}}, v_{\mathrm{rel}}\right) = \begin{cases} F_{\mathrm{N}}\mu r \operatorname{sgn}\left(v_{\mathrm{rel}}\right), & \left|\varphi_{i,j}q - x\right| < \beta_{\mathrm{S}}, \\ F_{\mathrm{N}}\mu r \operatorname{sgn}\left(v_{\mathrm{rel}}\right) + d v_{\mathrm{rel}}^{e} + c\left(\left|x_{\mathrm{rel}}\right| - \beta_{\mathrm{S}}\right)^{e} \operatorname{sgn}\left(x_{\mathrm{rel}}\right), & \left|\varphi_{i,j}q - x\right| \geq \beta_{\mathrm{S}}. \end{cases} \tag{6}$$

The relative angular speed v_{rel} and the relative angular displacement x_{rel} between the structure and the damper are $v_{\mathrm{rel}} = \varphi_{i,j}\dot{q} - \dot{x}$ and $x_{\mathrm{rel}} = \varphi_{i,j}q - x$ in the minimal model and $v_{\mathrm{rel}} = \dot{u}_{\mathrm{M,d}} - \dot{x}$ and $x_{\mathrm{rel}} = u_{\mathrm{M,d}} - x$ in the CMS reduced model. The equation of motion for the minimal model with a linear, nondissipating contact ($e = 1$ and $d = 0$) and a linearized torque characteristic at the bit that results in a negative modal damping ratio $D_i + D_{\mathrm{bit}} < 0$ is

$$\begin{pmatrix} 1 & 0 \\ 0 & J \end{pmatrix}\begin{pmatrix} \ddot{q} \\ \ddot{x} \end{pmatrix} + \begin{pmatrix} 2\left(D_i + D_{\mathrm{bit}}\right)\omega_{0,i} & 0 \\ 0 & 0 \end{pmatrix}\begin{pmatrix} \dot{q} \\ \dot{x} \end{pmatrix} + \begin{pmatrix} \omega_{0,i}^{2} & 0 \\ 0 & 0 \end{pmatrix}\begin{pmatrix} q \\ x \end{pmatrix} = \begin{pmatrix} -\varphi_{i,j}M\left(\varphi_{i,j}q - x, \varphi_{i,j}\dot{q} - \dot{x}\right) \\ M\left(\varphi_{i,j}q - x, \varphi_{i,j}\dot{q} - \dot{x}\right) \end{pmatrix}, \tag{7}$$

with a contact torque

$$M\left(q, x\right) = \begin{cases} F_{\mathrm{N}}\mu r \operatorname{sgn}\left(\varphi_{i,j}\dot{q} - \dot{x}\right), & \left|\varphi_{i,j}q - x\right| < \beta_{\mathrm{S}}, \\ F_{\mathrm{N}}\mu r \operatorname{sgn}\left(\varphi_{i,j}\dot{q} - \dot{x}\right) + c\left(\left|\varphi_{i,j}q - x\right| - \beta_{\mathrm{S}}\right) \operatorname{sgn}\left(\varphi_{i,j}q - x\right), & \left|\varphi_{i,j}q - x\right| \geq \beta_{\mathrm{S}}, \end{cases} \tag{8}$$

between the structure and the damper. In the following time domain simulations, the sign function is approximated by $\operatorname{sign}(x) \approx (2/\pi)a\tan((\pi/2)\kappa x)$, with $\kappa = 20000$ which corresponds to high slope values of the nonlinear torque characteristic at relative velocities near zero.

The presented torsional shock-friction damper, described mathematically in (7) and (8), is illustrated in Figure 3. Figure 3 shows the added torsional shock-friction damper (red), represented by a ring mass with a gap, and a section of the drill string (blue) that are connected via a friction contact. The damper can only move rotationally on the structure and is limited by a torsional stop of the structure located in the gap of the damper.

3. Investigation and Comparison of the Minimal and CMS Reduced Models

In the following section, the time domain results from the modal minimal model and the CMS reduced model are analyzed and compared. In particular, the reduction of the drill string from multiple-degree-of-freedom to a modal single-degree-of-freedom is analyzed regarding the qualitative and quantitative accuracy of the model. Similar to [12], the various states of dynamic motion between the damper and the structure are observed. These four stages are the sticking regime, the stick-slip (mixed) regime, the pure sliding regime, and the shock regime. In [12], the friction damper without backlash is analyzed, and the first three regimes are shown in detail. Figure 4 shows the angular velocity of the critical mode (modal coordinates) and the damper (physical coordinates) in the sliding regime, where no shocks occur. Only the friction torque acts between the structure and the damper. In this state, stable limit cycles occur when the additional damping provided by the damper exceeds the negative damping from the self-excitation.

In both cases, the exponential increase of the amplitude due to self-excitation is observable for low amplitudes. When the inertia moment exceeds the friction torque, the relative displacement occurs in the friction contact between the structure and the damper, resulting in dissipated energy and an increase of the damping. Figure 4 shows that the results from the CMS reduced and minimal models agree qualitatively and quantitatively. Hence, in this regime, the reduction to a single-degree-of-freedom is valid. Figure 5 shows the angular speed in the shock regime. Here, in both cases, the angular speed of the damper and the structure are

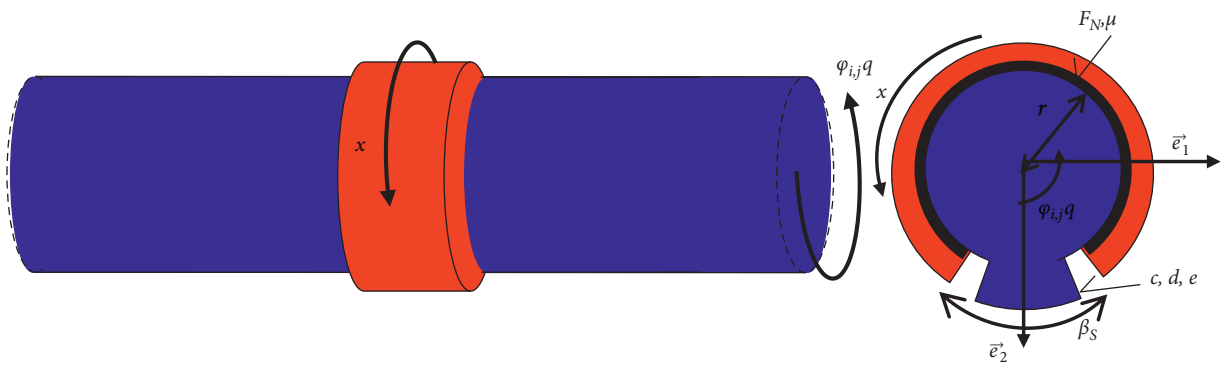

Figure 3: Principle sketch of a shock-friction damper in a drill string.

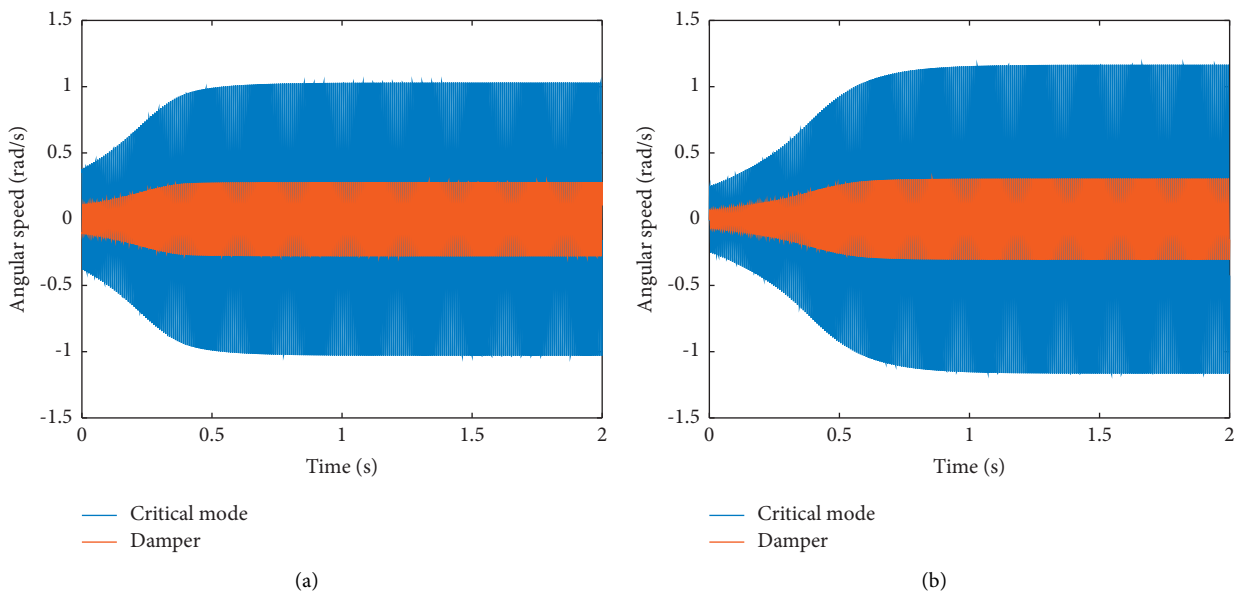

Figure 4: Time response of the damper (physical) and structure (modal) without shocks, using a CMS-reduced model (a) and a modal-reduced model (b).

shown in physical coordinates. The CMS reduced and the minimal model show, in contrast to Figure 4 and [12], the additional shock state. First, the amplitudes increase exponentially; then, a relative displacement occurs in the sticking and sliding (mixed regime) and the pure sliding regime, between the inertia damper and the contact point in the drilling system. If the additional damping provided by the damper is not sufficient to stabilize the system, the amplitudes related to the drilling system further increases. Hence, the amplitude of the structure further increases but, due to the additional damping, at a lower rate. Finally, the shock phase occurs where the relative angular displacement between the damper and the structure is higher than the backlash width. The resulting shocks can lead to high damping ratios and therefore a reduction of the amplitude of the critical mode. Subsequently, the phases repeat again.

Especially in the shock phase, the energy transferred between various modes of the CMS reduced model gives significant information about the importance of the other modes in the multiple-degree-of-freedom system. Figure 6 shows the modal energy of the five modes with the highest modal energy. A common phenomenon in drill string dynamics is that only one higher-order mode is unstable (self-excited). In the analyzed system, the fifth mode is self-excited. In Figure 6, the various phases are easily identified in the modal energy. First, an exponential increase of the modal energy (1) is observed. At some point, the additional damping from the damper reduces but does not stop the increase of the modal energy (2). The amplitude increases further, which leads to shocks (3). The shocks are shown in the modal energy by a sudden decrease of the modal energy of the critical mode (fifth mode). The other modes show a slight increase in the modal energy. Nevertheless, due to the small positive modal damping ratio and the high frequency of the other modes, the transferred modal energy is quickly dissipated, hence negligible.

These results show two major aspects. First, the nonlinear damper does influence other modes of the structure, especially in the shock phase, but these influences can be neglected here. In this case, the reason for the negligible

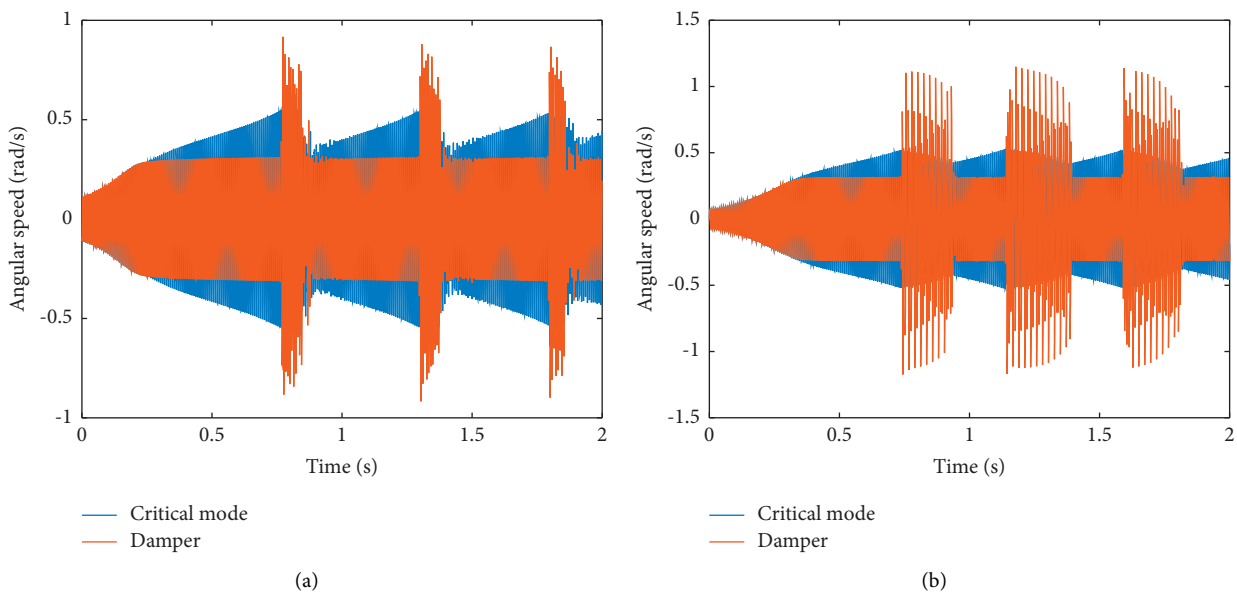

Figure 5: Time response of the damper (physical) and structure (physical amplitude at the damper) with shocks, using a CMS-reduced model (a) and a modal-reduced model (b).

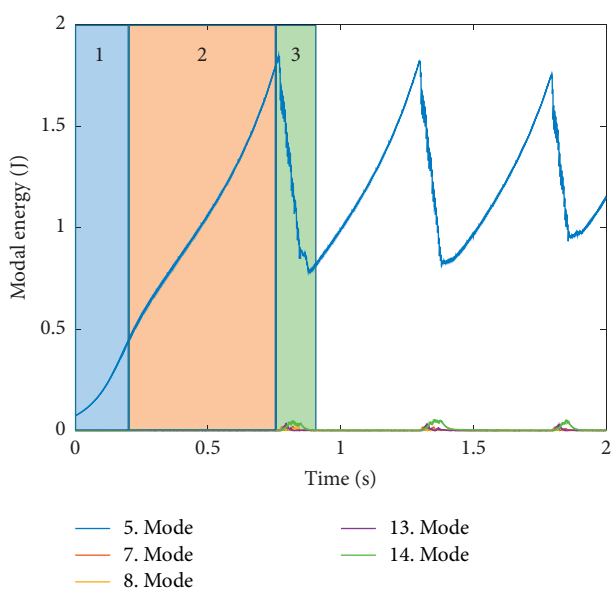

Figure 6: Modal energies of the five modes with the highest modal energy in the shock phase.

response of the other modes is a small mass-normalized eigenvector of the drill string modes at the damper location that directly influences the transfer of the shock to these modes. Second, the small quantitative differences between the two models can be attributed to the higher reactive effect of the damper on the overall dynamics of the structure in the minimal model. The response is highly dependent on the inertia of the connected damper and can lead to, e.g., a frequency-related detuning of the system, especially in the minimal model. As the diameter of the damper is limited through the borehole and tool diameter of the drilling system, only relatively small rotational inertia can be realized. This leads to a negligible effect of the damper on the dynamics (e.g., mode shape, natural frequency) of the system. In the following section, primarily the shock phase of the minimal model is examined in time domain.

4. Analysis of the Vibration Response and Energy Flow in Time Domain

By adjusting the parameters, all phases of the relative displacement can be observed. Figure 7(a) shows the angular speed of the structure and the damper in time domain derived with the minimal model similar to Figure 5. For small amplitudes, sticking occurs in the frictional contact between the damper and the drilling system and no relative movement between the structure and the damper can be observed. Due to the self-excitation ($D_i < 0$), energy periodically accumulates in the system (Figure 7(b)), resulting in an increase of the amplitude of the structure in the sticking phase. At a certain amplitude of the structure, the inertial torque of the damper is greater than the friction torque, $J\ddot{x} > F_N \mu r$, resulting in a relative displacement between the structure and the damper in the sliding regime, hence the energy dissipation in the friction contact. When the dissipated energy in the friction contact is not sufficient to stabilize the system, the amplitude further increases, which results in an increased relative displacement. When the relative displacement between the damper and the structure exceeds the backlash width, shocks occur between the damper and the structure.

These shocks, which do not occur in a conventional friction damper, lead to an energy transfer between the damper and the structure. Figure 7(b) shows that when a shock occurs, the energy is dissipated in the self-excited structure while the kinetic energy of the damper increases. This leads to two positive effects on the stability and energy

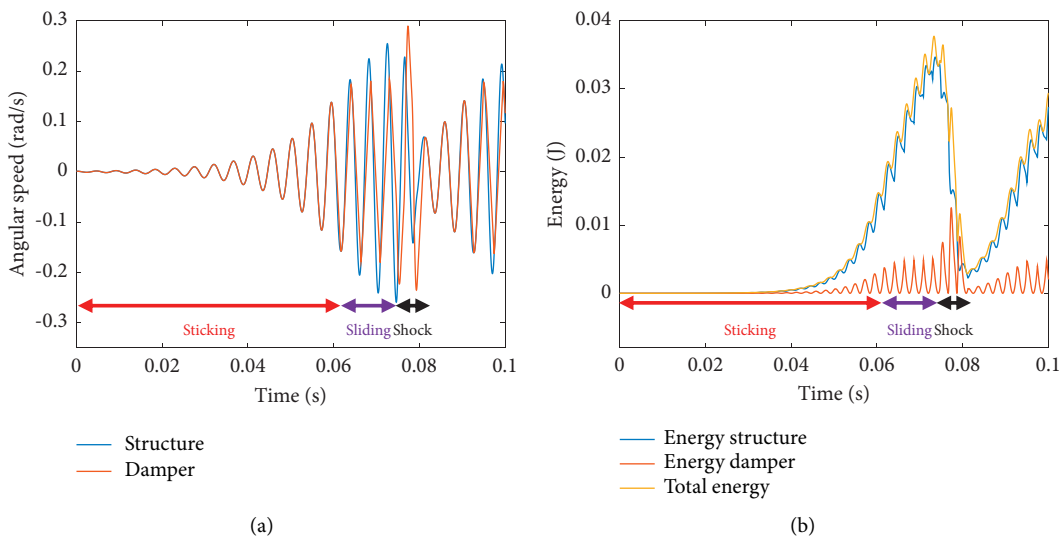

Figure 7: Time response of the damper and the structure (a); energy flow within the system (b).

output of the system. First, the energy transfer reduces the energy of the structure, resulting in a reduced amplitude and thus lower energy input due to self-excitation. Second, the energy transferred to the damper increases the relative angular speed between the damper and the structure, hence resulting in more energy dissipation in the friction contact. The first effect is rather indirect, as no energy is dissipated, but the energy flow into the system due to the self-excitation is reduced. The second effect is a direct dissipation through the friction contact between the structure and the damper. In this particular case with ($e = 1$ and $d = 0$), energy dissipation does not occur directly in the shock contact. To get a deeper understanding as well as to enable effective design and optimization strategies for the damper, the increased energy dissipation and damping related to the second effect are determined semi-analytically by using the harmonic balance method [36–38], hence assuming a constant harmonic motion of the structure.

5. Derivation of a Semi-Analytical Solution

Similar to [12], a semi-analytical solution for the shock-friction damper is derived from the minimal model by using the harmonic balancing method. To derive the semi-analytical solution from the minimal model, assumptions are made. The assumptions on which the minimal model is based are considered: one critical mode dominates the system dynamics at a time (shown in downhole data [6, 7]), the effect of the damper on the modal parameters of the structure is negligible (limited installation space [12]), and other modes are not excited due to friction or shock (no significant energy transfer Figure 6). It is further assumed that the influence of the damper torque on the dynamic movement of the structure is small and the oscillation of the structure is harmonic. In the friction regime where only friction occurs (Figure 4), a nearly harmonic motion with a constant amplitude can be observed in the time domain simulations. In contrast, Figures 5 and 7 show a transient response with strong changes in the amplitude due to the shocks. In the shock regime, the results from the semi-analytical solution have to be evaluated carefully. According to the harmonic balance method, the motion of the self-excited structure and its time derivations is modeled by

$$\begin{aligned} q &= \hat{q}\sin\left(\omega_{0,i}t\right), \\ \dot{q} &= \hat{q}\omega_{0,i}\cos\left(\omega_{0,i}t\right), \\ \ddot{q} &= -\hat{q}\omega_{0,i}^2\sin\left(\omega_{0,i}t\right), \end{aligned} \tag{9}$$

where $\hat{q}$ denotes the modal amplitude of the considered critical mode. For $|\varphi_{i,j}\hat{q}\sin(\omega_{0,i}t) - x| < \beta_S$, the relative displacement between the damper and the structure is smaller than the backlash angle β_S which results in the equation of motion

$$J\ddot{x} = F_N\mu r\,\mathrm{sgn}\left(\varphi_{i,j}\hat{q}\omega_{0,i}\cos\left(\omega_{0,i}t\right) - \dot{x}\right). \tag{10}$$

If $|\varphi_{i,j}\hat{q}\sin(\omega_{0,i}t) - x| \geq \beta_S$, the relative displacement is higher than the backlash, resulting in the equation of motion

$$J\ddot{x} = F_N\mu r\,\mathrm{sgn}\left(\varphi_{i,j}\hat{q}\omega_{0,i}\cos\left(\omega_{0,i}t\right) - \dot{x}\right) + c\left(\left|\varphi_{i,j}\hat{q}\sin\left(\omega_{0,i}t\right) - x\right| - \beta_S\right)\mathrm{sgn}\left(\varphi_{i,j}\hat{q}\sin\left(\omega_{0,i}t\right) - x\right). \tag{11}$$

Using (10) and (11), the steady-state motion of the damper x and the torque $M(q, x)$ between the damper and the structure are determined semi-analytically (by approximating the sgn function) or by sectional linearization

(Appendix). With this information, the equivalent damping of the damper on the structure is determined by averaging the dissipated energy E_d over one period. Following the averaging of the dissipated energy, the equivalent damping D_{eq} is determined by transferring the dissipated energy E_d from the nonlinear contact to a linear modal damping. For a harmonic motion of the mode representing the structure, the damping ratio D_{eq} is further simplified

$$D_{eq} = \frac{E_d}{2\omega_{0,i}\int_0^T \dot{q}^2 dt} = \frac{E_d}{2\pi\omega_{0,i}^2\dot{q}^2}. \quad (12)$$

In [12], this method is used to derive an analytical and semi-analytical solution for a friction damper without shocks (equation (10)). Figure 8 shows a damping diagram for a friction damper (adjusted/normalized to 1% maximum damping). The analytical solution for the maximum equivalent damping $D_{eq,max} = (2/\pi^2)\varphi_{i,j}^2 J$, the amplitude where this maximum damping occurs $\hat{q}_{max} = (\pi F_N \mu r/\sqrt{2}\varphi_{i,j} J\omega_{0,i}^2)$, and the amplitude from which on sliding occurs $\hat{q}_{slid} = (F_N \mu r/\varphi_{i,j} J\omega_{0,i}^2)$ can be determined from the analytic results. These equations can be used to optimize the design of one or multiple friction dampers regarding various parameters, e.g., the provided damping, the effective amplitude range, and the positioning. Despite the analytical solutions, the dynamic motion in the mixed regime is determined semi-analytically.

Similar to Figure 8, a damping diagram for the shock-friction damper is determined as shown in Figure 9. In addition to the states of the friction damper without backlash (sticking-only, mixed, and sliding-only), Figure 9 shows the shock state. In the shock state, the additional damping provided by the damper is increased. The sudden increase of the damping corresponds to the increased dissipated energy in the friction contact due to the increased relative velocity due to the increase in kinetic energy shown in Figure 7(b).

Figure 9 shows that prior to the shock regime, both the friction and the shock-friction damper exhibit the same dynamic response. This is the case because when the modal amplitude of the underlying structure is small, the backlash width is not exceeded by the relative motion between the damper and the structure, i.e., no shocks occur.

6. Design and Parameter Sensitivity

One important design parameter of the shock-friction damper is the backlash width. The size of the backlash width determines the amplitude at which shocks and thus the energy transfer between the damper and the structure occur. Figure 10 shows the damping effect of the shock-friction damper for a specific design with variations of the backlash width.

The backlash limits the relative movement between the damper and the underlying structure. In the sticking regime, neither friction damping nor shocks occur. When the amplitude increases, this leads to relative motion between the structure and the damper, resulting in sliding

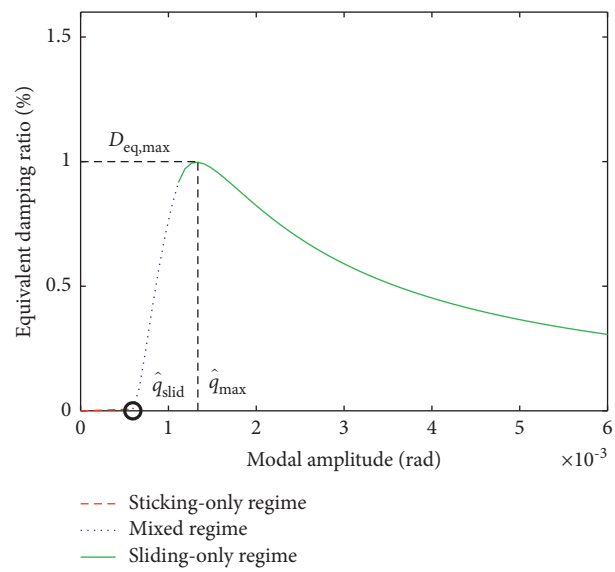

Figure 8: Semi-analytically determined damping diagram for a friction damper c.f. [12].

and thus an increased damping. Without the backlash, this leads to the underlying friction damping related curve (Figure 10 (black curve)). The additional shock damping is effective if the relative motion between the inertia damper and the structure exceeds the backlash width. The additional damping through the shocks with the mechanism described above is leading to a discontinuous damping curve in the transition from sliding friction to sliding friction with shocks. The amplitude of this discontinuity depends on the backlash width as observed in Figure 10. When the mechanical backlash width is too small, the movement of the damper is limited by the backlash. This limits the relative motion, resulting in a reduction of the dissipated energy and damping. For large backlash widths, the energy transfer from the structure to the damper due to the shocks occurs at high amplitudes. Although this results in a higher dissipated energy, the occurring higher amplitudes correspond to a lower damping ratio. The reason is that the damping is a ration between the dissipated energy and the corresponding amplitude. The optimal backlash width corresponds to the relative displacement amplitude near the maximum damping ratio of the friction damper (Figure 10 (black curve)). Near this amplitude, the proportion of the relative displacement, the friction torque, and the amplitude of the structure is leading to high equivalent modal damping ratios. To determine the optimum backlash width, an analytical equation for the rough design of the backlash width (angle β_s) of the shock-friction damper is derived. The maximum damping of the friction damper without backlash is in the sliding-only regime (Figure 8 and [12]). Here, the relative displacement $x_{rel} = x(t) - \varphi_{i,j}\hat{q}\sin(\omega t_1)$ can be solved analytically. In [12], the relative velocity in the sliding-only regime was solved analytically. To determine the relative

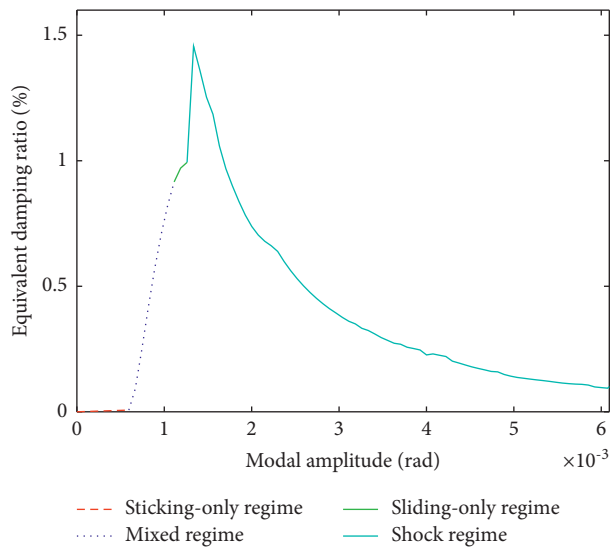

Figure 9: Semi-analytic determined damping diagram for a shock-friction damper.

displacement over half a period $(\pi/\omega_{0,i})$, the analytical solution for the relative velocity is

$$v_{\mathrm{rel}} = \pm \frac{F_{\mathrm{N}}\mu r}{J}(t - t_1) + \varphi_{i,j}\omega_{0,i}\hat{q}\cos(\omega_{0,i}t_1) - \varphi_{i,j}\hat{q}\omega_{0,i}\cos(\omega_{0,i}t), \tag{13}$$

and the time

$$t_1 = \frac{\arccos\left(\left(\pi F_{\mathrm{N}}\mu r/2J\hat{q}\varphi_{i,j}\omega_{0,i}^2\right)\right)}{\omega_{0,i}}, \tag{14}$$

where the friction torque $F_{\mathrm{N}}\mu r$ changes the sign are integrated over half a period. Thus, the total distance traveled over half a period of pure sliding is determined. At the physical amplitude of the maximum damping of the friction damper without shock $\varphi_{i,j}\hat{q}_{\max}$ (Figure 9), shocks should occur for optimal utilization of the backlash. This means that the total relative displacement at this amplitude should be equal to the total backlash angle $2\beta_{\mathrm{S}}$. Thus, via

$$\int_{t_1}^{t_1+(\pi/\omega_{0,i})} v_{\mathrm{rel}}(\hat{q}_{\mathrm{opt}}, t)\mathrm{d}t = \int_{t_1}^{t_1+(\pi/\omega_{0,i})} -\frac{F_{\mathrm{N}}\mu r}{J}(t - t_1) + \varphi_{i,j}\omega_{0,i}\frac{\pi F_{\mathrm{N}}\mu r}{\sqrt{2}\varphi_{i,j}J\omega_{0,i}^2}\cos(\omega_{0,i}t_1) - \varphi_{i,j}\frac{\pi F_{\mathrm{N}}\mu r}{\sqrt{2}\varphi_{i,j}J\omega_{0,i}^2}\omega_{0,i}\cos(\omega_{0,i}t)\mathrm{d}t = 2\beta_{\mathrm{S}}, \tag{15}$$

the backlash angle (backlash width)

$$\beta_{\mathrm{S}} = \frac{F_{\mathrm{N}}\mu r\pi}{2J\omega^2}, \tag{16}$$

is determined. The other parameters like the inertia of the damper mass or positioning of the damper (mass-normalized modal amplitude at the friction contact) have a similar influence on the damping effect of the shock-friction damper as for the friction damper. Thus, both a higher damper inertia and especially a better positioning (higher mass-normalized modal amplitude) increase the damping effect. Similar results are shown in Figure 11. Similar to the conventional friction damper the friction torque, the coefficient of friction, the friction radius and the normal force do not influence the equivalent damping for an optimized backlash (equation (16)). The friction torque only scales the amplitude where the damping maximum occurs.

Unlike for the friction damper, the frequency has an influence on the damping effect of the shock-friction damper. Figure 12 shows the influence of the natural frequency of the underlying structure on the damping effect of the damper for a design where the backlash width is adjusted according to equation (16).

Figure 12 shows that the damping effect increases with an increasing frequency. This effect corresponds to a change in the stiffness c of the mechanical backlash contact. The stiffness and the natural frequency of the structure can be tuned. The optimum can be attributed to the absorber frequency $\omega_{0,i} \approx \sqrt{c/J}$. With this information, a rough

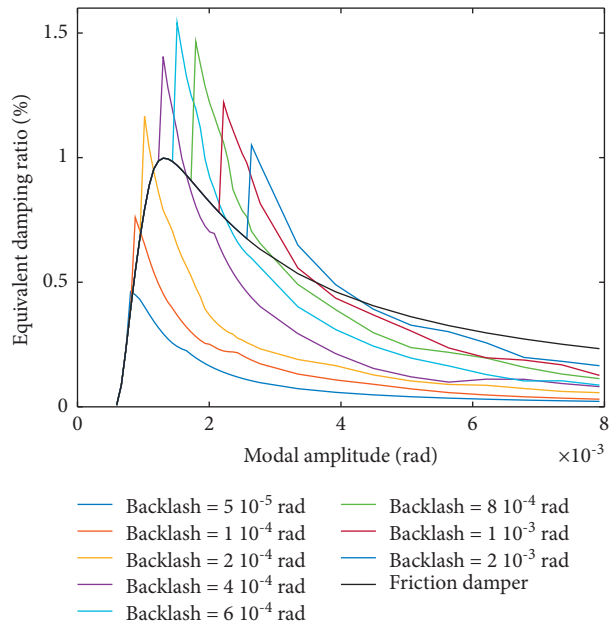

Figure 10: Influence of the mechanical backlash on the damping effect of the shock-friction damper.

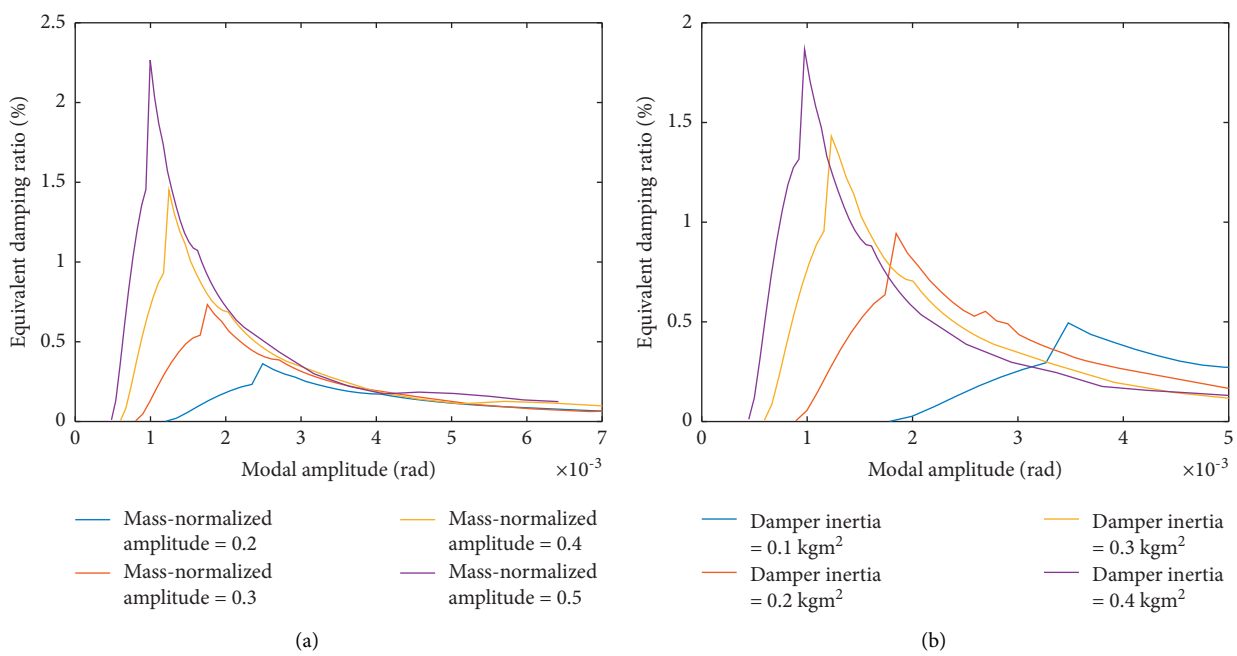

Figure 11: Influence of the mass-normalized modal amplitude at the damper (a) and the rotational inertia of the damper (b) on the equivalent damping ratio.

design of the damper is created. In highly nonlinear systems, the initial values have an influence on the system dynamic. Due to the mechanical backlash, the position of the damper relative to the structure is decisive. Depending on the position, shocks can occur even at very small amplitudes. The equations (Appendix) show that each shock causes a change in the angular speed of the damper. This can lead to a new solution of the steady state due to a change of the initial values. Figure 13 shows the damping effect of the shock-friction damper for two different initial conditions. The initial relative displacements between the structure and the damper are different. The initial condition where the damper is closer to one side of the mechanical backlash shows higher damping ratios at lower modal amplitudes. This is the case because at small amplitudes no shocks occur between the damper and the structure but due to the smaller initial relative displacements between the damper and the backlash, the shocks occur at smaller amplitudes. Although the friction torque would not be sufficient to surpass the backlash width, a

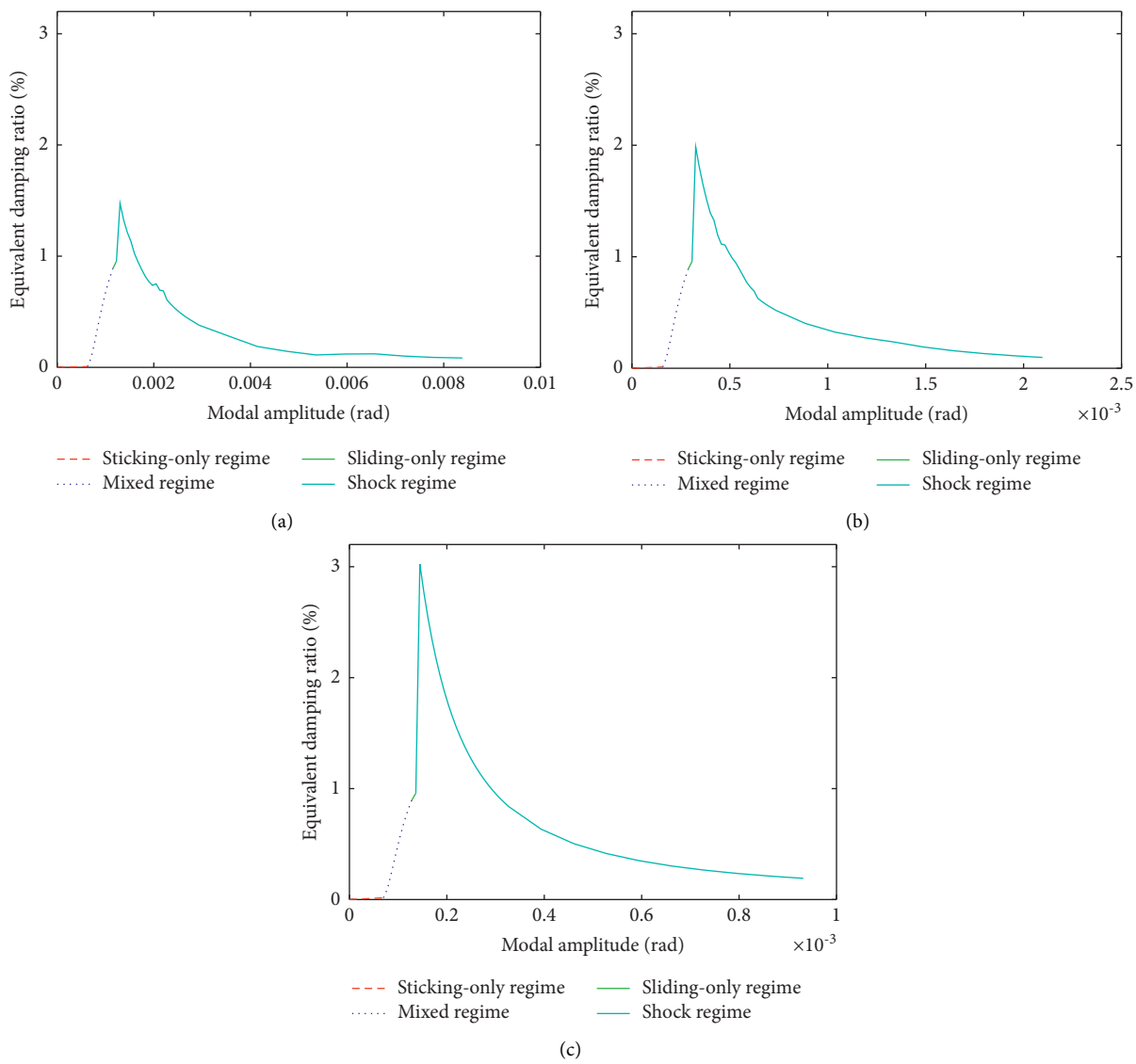

Figure 12: Influence of the natural frequency of the structure on the damping effect of the shock-friction damper (a) $f = 130$ Hz, (b) $f = 260$ Hz, and (c) $f = 390$ Hz with optimized backlash width.

steady state is reached because the shock itself increases the angular speed of the damper mass and thus the backlash width can be surpassed.

This can influence the damping effect and design of the damper. Therefore, the rough design using (16) should be improved by using the semi-analytical solution and, if necessary, extended by considering the uncertainties regarding the initial conditions as well as finally transferring the damper to self-excited systems. Figure 14 shows four different solutions for various amplitudes of the underlying structure, from simple T-periodic solutions with and without shocks (Figures 14(a) and 14(b)) to multiple nT-periodic solutions (Figure 14(c)) up to not periodic solutions (Figure 14(d)). The initial conditions have no influence on the equivalent damping when no shocks occur (Figure 14(a)).

Figure 14 shows the complexity of the dynamic motion, especially in the shock regime, because all possible states can occur in one period (shock, sliding, and sticking). Only steady-state solutions similar to Figure 14(a) can occur in the self-excited system. The other solutions in Figure 14 arise at amplitudes higher than the amplitude of the maximal damping, hence in self-excited systems these solutions are not observed and would represent an unstable solution.

7. Transfer to Self-Excited Drill String Vibrations

In the following section, the damping diagram from the semi-analytical solution is related to self-excited systems. Figure 15 shows the damping diagram of a shock-friction damper. Additionally, in Figure 15, three cases of self-excitation are shown that are modeled and varied by the absolute value of linearized negative damping ratios. The absolute value of the two self-excited damping ratios ($D_i = -0.7\%$, $D_i = -1.2\%$) result in intersections between

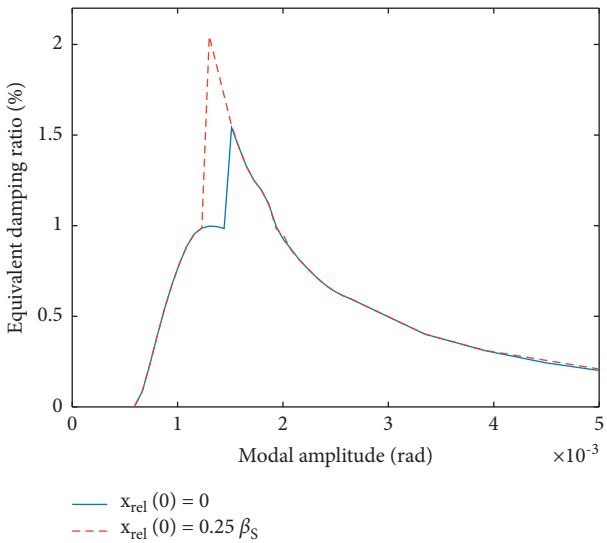

Figure 13: Influence of the initial values on the damping effect of the shock-friction damper.

the self-excitation and the damping provided by the damper. The absolute value of the third self-excitation ($D_i = -1.5\%$) is higher than the maximum damping provided by the damper and therefore no intersections occur.

Figure 16 shows the corresponding time domain results of the self-excited system. For all cases, an exponential increase for small amplitudes is shown that is corresponding to the sticking regime of a friction damper. For minor self-excitations (instability of $D_i = -0.7\,\%$), a steady state with a constant amplitude of the angular displacement of the structure is observed (Figure 16(a)), no shocks occur, and the damping effect related to friction is sufficient to stabilize the system. The stable limit cycle of Figure 16(a) is similar to the one with friction damping only in Figure 14(a). The amplitude of the angular displacement of the critical mode is similar to the modal amplitude at the intersection of the corresponding self-excitation with the provided damping in Figure 15, hence the damping diagram not only shows the provided damping but also the occurring amplitude of the limited cycle. When a system is self-excited, the amplitude increases until the energy balance is zero (dissipated energy $E_d = E_s$ self-excited energy) and a limited cycle occurs. In Figure 16(b), the energy input through self-excitation is increased to $D_i = -1.2\%$, resulting in a higher necessary damping to stabilize the system. The friction damping mechanism alone cannot provide sufficiently high additional damping to achieve a stable limit cycle with an acceptable amplitude. The additional shock phase increases the damping. This sudden increase of the damping leads to two major phases. First, for smaller amplitudes before the shocks occur, the self-excited energy E_s is higher than the dissipated energy in the friction contact E_d ($E_d < E_s$), leading to a positive energy balance and therefore an increase of the amplitude of the structure. At some point, the amplitude at which shocks occur is reached, and therefore, the additional damping provided by the damper is increased significantly. The sudden increase leads to an increase of the dissipated energy and thus a negative energy balance $E_d > E_s$. The rapid increase of the dissipated energy results in a sudden decrease of the amplitude of the structure. The decrease of the amplitude of the structure results in a decrease of the relative motion and thus an end of the shock phase and therefore a reduced additional damping. This means that, similar to the beginning, the energy input due to the self-excitation is larger than the damping provided by the damper ($E_d < E_s$). Therefore, the energy balance is positive, and the vibration amplitude of the structure increases until the shock range is reached again. In this context, the position of the damper relative to the structure is crucial. The new position can result in an increased or decreased damping ratio during the next shock phase. Therefore, the previously made considerations regarding the position of the damper relative to the structure are decisive (Figure 13), and the minimum damping ratio should be taken into account in the design.

Finally, the last case, the unstable case, is shown in Figure 16(c). Here the damping provided by the damper is neither in the friction nor in the shock phase sufficient to stabilize the unstable mode. For a linearized minimal model, this results in an exponential increase of the amplitude. In a real, not linearized system, a maximum amplitude is reached. In drill string dynamics, this maximum amplitude, which corresponds to the maximum limited cycle, is dependent on the average rotary speed ν_{RPM}(RPM, revolutions per minute) of the drill string. In [9, 11], an analytical solution for the maximum amplitude $\varphi_{i,bit}\hat{q} = (2\pi\,\nu_{RPM}/60\ \omega_{0,i})$ was determined. These results show how the information of the semi-analytical solution can be transferred to the self-excited system.

Following this, any self-excited vibration with corresponding energy inputs lower than the maximum damping shown in Figure 15 is stabilized by the shock-friction damper. Due to the assumptions and approximations done to determine the semi-analytical solution and due to the small stable area at the maximum, this is not exactly the case. Self-excitation results in an increase of the amplitude. When this increase is higher than the stable area, the stabilizing effect of a damper can be undermined ("skipped"). The accuracy of the solution is highly dependent on the reactive effect of the damper on the modes of the structure. The reactive effect increases with the inertia J and mass-normalized amplitude at the point where the damper is connected to the structure $\varphi_{i,j}$. Due to the limited installation space in drilling systems that are naturally confined by the borehole size, the inertia J is rather small. Additionally, the mass-normalized amplitude of a drill string is, due to the high inertia of the structure, small. Hence, in general, the modal amplitude is two, three, or four times higher than the physical amplitude. This means that the excitability is low and thus the effects of the shocks on other modes are low. In the field of drill string dynamics, the semi-analytical results and the design equations are sufficiently accurate. The results can also be transferred to other dynamic systems where one mode dominates the system response and the reactive effect can be neglected.

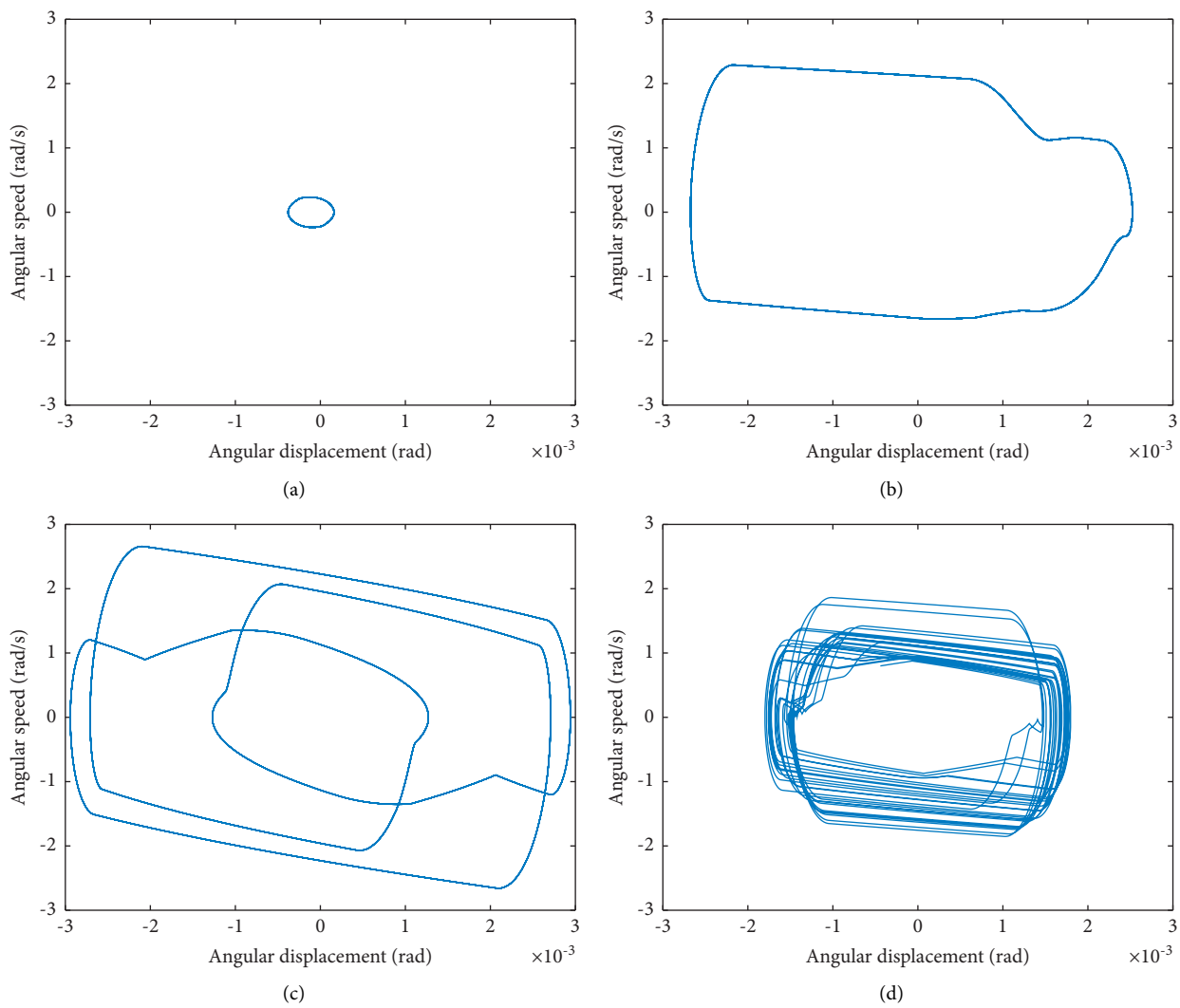

Figure 14: Phase space of the shock-friction damper for different steady-state solutions (various excitation amplitudes of the underlying structure) (a) limit cycle without shocks, (b) T-periodic limit cycle with shocks, (c) 3T-period, and (d) not periodic attractor.

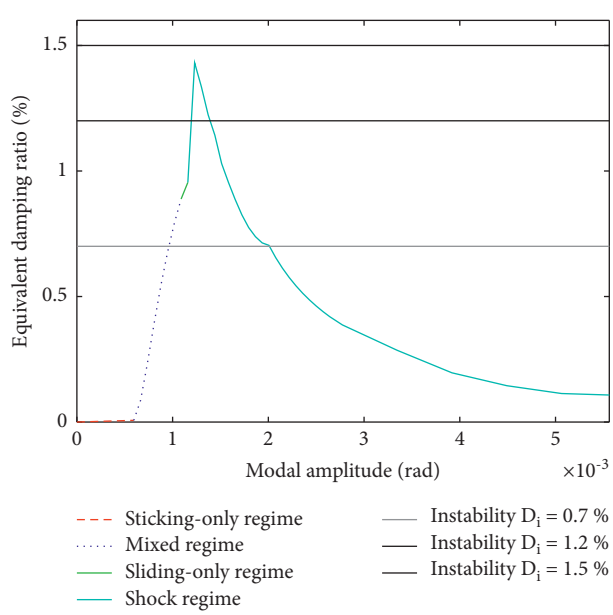

Figure 15: Semi-analytic determined damping diagram for a shock-friction damper with instabilities.

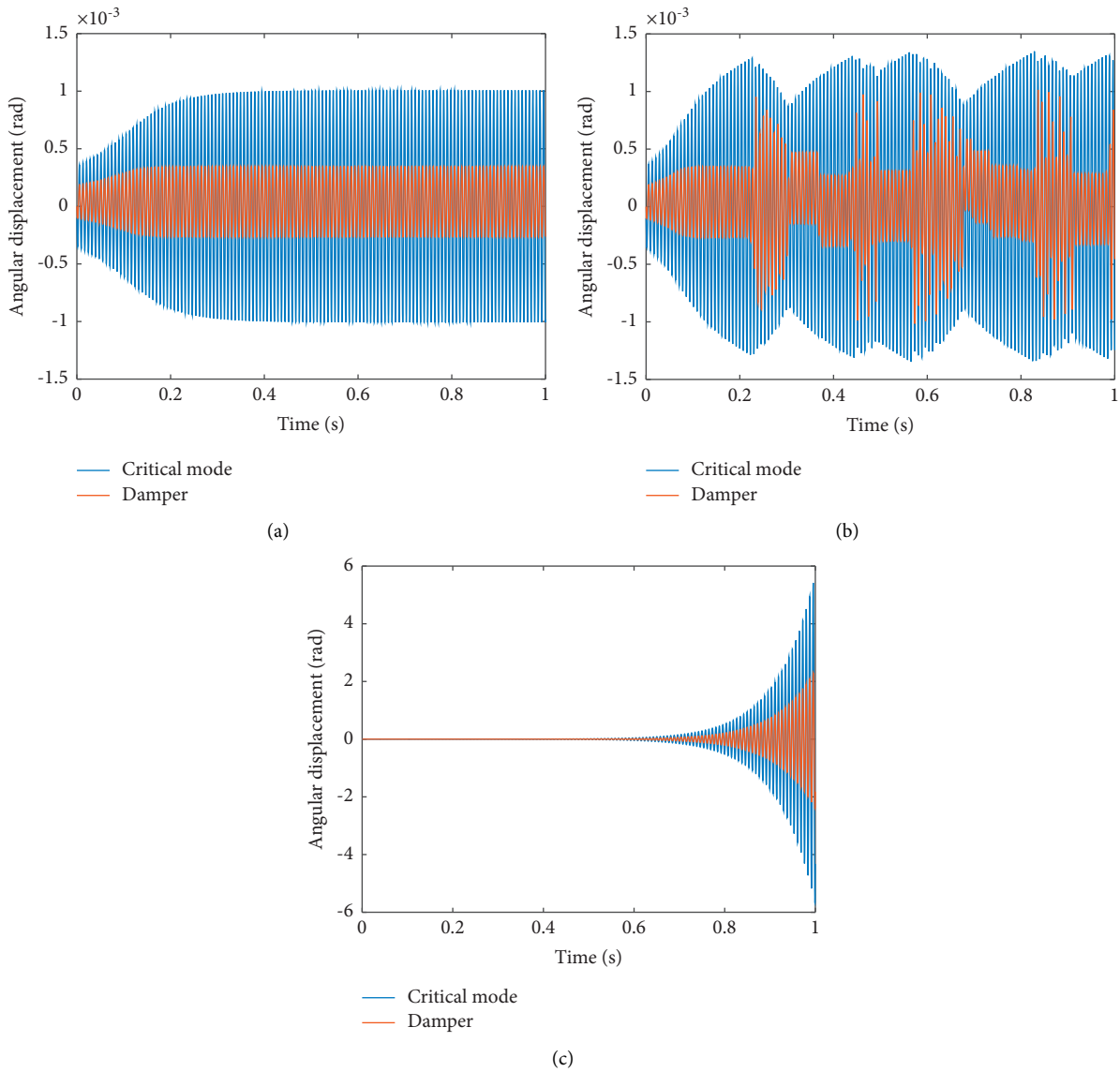

Figure 16: Time domain results from the self-excited minimal model for (a) $D_i = 0.7\%$, (b) $D_i = 1.2\%$, and (c) $D_i = 1.5\%$.

8. Conclusions

In this paper, a damper based on friction and shock is analyzed regarding its suitability to reduce self-excited HFTO in downhole drilling systems. A semi-analytical solution based on the harmonic balance is derived and compared with time domain simulations of a minimal model and an extended CMS reduced model. The semi-analytical solution is used to determine the damping that is provided by the damper for various parameters, e.g., the amplitude. This enables efficient optimization and design strategies regarding, e.g., position within the BHA, friction torque, and backlash width and reduces complex time domain simulations and stability analysis. An analytical equation to roughly design the backlash width of the nonlinear damper and influence its effective amplitude range is derived from the semi-analytical solution. Finally, the results are transferred to self-excited drill string vibration, and the characteristics are examined in detail, showing the accuracy and usability of the results. The combination of friction and backlash results in passive shocks, causing energy transfer between the self-excited structure and the damper that positively influences the energy output of the system. Compared to a conventional friction damper without backlash, an increase in the damping effect is achieved by adjusting the normal force and backlash width regarding the vibration frequency.

Appendix

Through sectional linearization, a semi-analytical solution is determined for the shock-friction damper. The seven different equations of motion consist of the sticking equation, two pure sliding equations, and four shock equations with various signs of the friction- and shock-torque. In the sliding regime for $|\varphi_{i,j}\hat{q}\sin(\omega_{0,i}t) - x| < \beta_S$, the differential equation (equation (10))

$$J\ddot{x} = F_{\mathrm{N}}\mu r\,\mathrm{sgn}\left(\varphi_{i,j}\widehat{q}\omega_{0,i}\cos\left(\omega_{0,i}t\right) - \dot{x}\right), \tag{A.1}$$

is solved depending on the relative velocity by

$$\begin{aligned} x(t) &\\ \dot{x}(t) &= \pm\frac{F_{\mathrm{N}}\mu r}{J}\left(t - t_0\right) + \dot{x}\left(t_0\right), \\ \ddot{x}(t) &= \pm\frac{F_{\mathrm{N}}\mu r}{J}. \end{aligned} \tag{A.2}$$

For the shock regime, hence $|\varphi_{i,j}\widehat{q}\sin(\omega_{0,i}t) - x| \geq \beta_{\mathrm{S}}$ the differential equation (equation (11))

$$J\ddot{x} = F_{\mathrm{N}}\mu r\,\mathrm{sgn}\left(\varphi_{i,j}\widehat{q}\omega_{0,i}\cos\left(\omega_{0,i}t\right) - \dot{x}\right) + c\left(\left|\varphi_{i,j}\widehat{q}\sin\left(\omega_{0,i}t\right) - x\right| - \beta_{\mathrm{S}}\right)\mathrm{sgn}\left(\varphi_{i,j}\widehat{q}\sin\left(\omega_{0,i}t\right) - x\right), \tag{A.3}$$

is solved depending on the relative velocity and the relative displacement through $J\ddot{x} + cx = \pm F_{\mathrm{N}}\mu r \pm \beta_{\mathrm{S}}c + c\,\varphi_{i,j}\widehat{q}\sin(\omega_{0,i}t)$ resulting in

$$\begin{aligned} x(t) &= \frac{\left(\pm F_{\mathrm{N}}\mu r \pm \beta_{\mathrm{S}}c\right)}{c} + \frac{c\varphi_{i,j}\widehat{q}}{c - \omega^2 J}\sin\left(\omega\left(t - t_1\right)\right) + A\,\sin\left(\sqrt{\frac{c}{J}}\left(t - t_1\right)\right) + B\,\cos\left(\sqrt{\frac{c}{J}}\left(t - t_1\right)\right), \\ \dot{x}(t) &= \frac{c\varphi_{i,j}\widehat{q}\omega}{c - \omega^2 J}\cos\left(\omega\left(t - t_1\right)\right) + A\sqrt{\frac{c}{J}}\cos\left(\sqrt{\frac{c}{J}}\left(t - t_1\right)\right) - B\sqrt{\frac{c}{J}}\sin\left(\sqrt{\frac{c}{J}}\left(t - t_1\right)\right), \end{aligned} \tag{A.4}$$

where A and B are determined by

$$\begin{aligned} A &= \frac{1}{\sqrt{c/J}}\left(\dot{x}\left(t_0\right) - \frac{c\varphi_{i,j}\widehat{q}\omega}{c - \omega^2 J}\right), \\ B &= x\left(t_0\right) - \frac{\left(\pm F_{\mathrm{N}}\mu r \pm \beta_{\mathrm{S}}c\right)}{c}, \end{aligned} \tag{A.5}$$

and dependent on the initial condition $x(t_0)$ and $\dot{x}(t_0)$ at time t_0 were the new section starts. The final equation is the sticking equation where no relative velocity occurs, hence $\dot{x}(t) = \varphi_{i,j}\omega_{0,i}\widehat{q}\cos(\omega_{0,i}t)$.

Data Availability

The data used to support the findings of this study are included within the article.

Conflicts of Interest

The authors declare that there are no conflicts of interest regarding the publication of this paper.

Acknowledgments

The authors would like to thank Baker Hughes for supporting the work and giving permission to publish this paper. We acknowledge support by the Open Access Publication Funds of the TU Braunschweig.

References

[1] H. Reckmann, P. Jogi, F. T. Kpetehoto, S. Chandrasekaran, and J. Macpherson, "MWD failure rates due to drilling dynamics," in *Proceedings of the IADC/SPE Drilling Conference and Exhibition*, New Orleans, Louisiana, USA, February 2010.

[2] A. I. Bowler, L. Logesparan, J. Sugiura, B. P. Jeffryes, R. J. Harmer, and M. Ignova, "Continuous high-frequency measurements of the drilling process provide new insights into drilling system response and transitions between vibration modes," in *Proceedings of the SPE Annual Technical Conference and Exhibition*, Amsterdam, The Netherlands, October 2014.

[3] H. Oueslati, J. R. Jain, H. Reckmann, L. W. Ledgerwood, R. Pessier, and S. Chandrasekaran, "New insights into drilling dynamics through high-frequency vibration measurement and modeling," in *Proceedings of the SPE Annual Technical Conference and Exhibition*, New Orleans, LA, USA, September 2013.

[4] J. R. Jain, H. Oueslati, A. Hohl et al., "High-frequency torsional dynamics of drilling systems: an analysis of the bit-system interaction," in *Proceedings of the IADC/SPE Drilling Conference and Exhibition*, Fort Worth, TX, USA, March 2014.

[5] H. Dennis, W. Mathäus, H. Christian, A. Hohl, and R. Hanno, "High-frequency torsional oscillation laboratory testing of an entire bottom hole assembly," in *Proceedings of the Abu Dhabi International Petroleum Exhibition & Conference*, Abu Dhabi, UAE, November 2017.

[6] A. Hohl, C. Herbig, P. Arevalo, H. Reckmann, and J. Macpherson, "Measurement of dynamics phenomena in

downhole tools–requirements, theory and interpretation," in *Proceedings of the IADC/SPE Drilling Conference and Exhibition*, Fort Worth, TX, USA, March 2018.

[7] H. Andreas, P. Eric, and A. Pedro, "Real-time system to calculate the maximum load of high-frequency torsional oscillations independent of sensor positioning," in *Proceedings of the SPE/IADC International Drilling Conference and Exhibition*, Hague, The Netherlands, 2019.

[8] A. Hohl, M. Tergeist, H. Oueslati et al., "Derivation and experimental validation of an analytical criterion for the identification of self-excited modes in drilling systems," *Journal of Sound and Vibration*, vol. 342, pp. 290–302, 2015.

[9] A. Hohl, M. Tergeist, H. Oueslati et al., "Prediction and mitigation of torsional vibrations in drilling systems," in *Proceedings of the IADC/SPE Drilling Conference and Exhibition*, Fort Worth, TX, USA, March 2016.

[10] A. Hohl, V. Kulke, A. Kueck, C. Herbig, G. Ostermeyer, and H. Reckmann, "The nature of the interaction between stick/slip and high-frequency torsional oscillations," in *Proceedings of the IADC/SPE International Drilling Conference and Exhibition*, Galveston, TX, USA, February 2020.

[11] A. Hohl, V. Kulke, A. Kueck et al., "Best practices for operations in HFTO prone applications," in *Proceedings of the SPE Asia Pacific Oil & Gas Conference and Exhibition*, Kuala Lumpur, Malaysia, November 2020.

[12] V. Kulke, G.-P. Ostermeyer, M. Tergeist, and A. Hohl, "Semi-analytical approach for derivation of an equivalent modal friction-damping ratio and its application in a self-excited drilling system," *Dynamics, Vibration, and Control*, vol. 4, 2019.

[13] V. Kulke, P. Thunich, F. Schiefer, and G.-P. Ostermeyer, "A Method for the design and optimization of nonlinear tuned damping concepts to mitigate self-excited drill string vibrations using multiple scales lindstedt-poincaré," *Applied Sciences*, vol. 11, no. 4, Article ID 1559, 2021.

[14] D. Heinisch, V. Kulke, V. Peters, C. Schepelmann, H. Reckmann, and G.-P. Ostermeyer, "Simulation and testing of an isolator tool for high-frequency torsional oscillation," in *Proceedings of the Abu Dhabi International Petroleum Exhibition & Conference*, November 2018.

[15] V. Kulke and G.-P. Ostermeyer, "Energy transfer through parametric excitation to reduce self-excited drill string vibrations," *Journal of Vibration and Control*, vol. 43, no. 1, 2021.

[16] A. Tondl, "To the problem of self-excited vibration suppression," *Engineering Mechanics*, vol. 15, no. 4, pp. 297–307, 2008.

[17] A. Tondl, "Quenching of self-excited vibrations equilibrium aspects," *Journal of Sound and Vibration*, vol. 42, no. 2, pp. 251–260, 1975.

[18] A. Tondl, "Quenching of self-excited vibrations: effect of dry friction," *Journal of Sound and Vibration*, vol. 45, no. 2, pp. 285–294, 1976.

[19] K. Popp, L. Panning, and W. Sextro, "Vibration damping by friction forces: theory and applications," *Journal of Vibration and Control*, vol. 9, no. 3-4, pp. 419–448, 2003.

[20] J. H. Griffin, "Friction damping of resonant stresses in gas turbine engine airfoils," *Journal of Engineering for Power*, vol. 102, no. 2, pp. 329–333, 1980.

[21] I. López, J. M. Busturia, and H. Nijmeijer, "Energy dissipation of a friction damper," *Journal of Sound and Vibration*, vol. 278, no. 3, pp. 539–561, 2004.

[22] I. Lopez and H. Nijmeijer, "Prediction and validation of the energy dissipation of a friction damper," *Journal of Sound and Vibration*, vol. 328, no. 4-5, pp. 396–410, 2009.

[23] A. F. Vakakis, L. A. Bergman, O. V. Gendelman, D. M. McFarland, G. Kerschen, and Y. S. Lee, *Nonlinear Targeted Energy Transfer in Mechanical and Structural Systems*, Springer Netherlands, Dordrecht, Netherlands, 2009.

[24] O. V. Gendelman, "Targeted energy transfer in systems with external and self-excitation," *Proceedings of the Institution of Mechanical Engineers - Part C: Journal of Mechanical Engineering Science*, vol. 225, no. 9, pp. 2007–2043, 2011.

[25] T. Pumhössel, "Suppressing self-excited vibrations of mechanical systems by impulsive force excitation," *Journal of Physics: Conference Series*, vol. 744, Article ID 12011, 2016.

[26] M. F. Dimentberg and D. V. Iourtchenko, "Random vibrations with impacts: a review," *Nonlinear Dynamics*, vol. 36, no. 2–4, pp. 229–254, 2004.

[27] S. Ema and E. Marui, "A fundamental study on impact dampers," *International Journal of Machine Tools and Manufacture*, vol. 34, no. 3, pp. 407–421, 1994.

[28] K. Duffy, R. Bagley, and O. Mehmed, "On a self-tuning impact vibration damper for rotating turbomachinery," in *Proceedings of the 36th AIAA/ASME/SAE/ASEE Joint Propulsion Conference and Exhibit*, p. 539, American Institute of Aeronautics and Astronautics, Reston, VA, USA, 2000.

[29] S. F. Masri and T. K. Caughey, "On the stability of the impact damper," *Journal of Applied Mechanics*, vol. 33, no. 3, pp. 586–592, 1966.

[30] J. Cheng and H. Xu, "Inner mass impact damper for attenuating structure vibration," *International Journal of Solids and Structures*, vol. 43, no. 17, pp. 5355–5369, 2006.

[31] B. Brogliato, *Nonsmooth Impact Mechanics: Models, Dynamics and Control*, Springer, Berlin, Germany, 1996.

[32] O. V. Gendelman and A. Alloni, "Forced system with vibro-impact energy sink: chaotic strongly modulated responses," *Procedia IUTAM*, vol. 19, pp. 53–64, 2016.

[33] R. R. Craig and M. C. C. Bampton, "Coupling of substructures for dynamic analyses," *AIAA Journal*, vol. 6, no. 7, pp. 1313–1319, 1968.

[34] J. Wijker, *Mechanical Vibrations in Spacecraft Design*, Springer, Berlin, Germany, 2004.

[35] M. A. d. Araújo Nunes and M. A. Viana Duarte, "Component mode synthesis method applied to two-dimensional acoustic analysis in ducts," *Journal of Vibration and Acoustics*, vol. 135, no. 1, p. 243, 2013.

[36] W.-J. Kim and N. C. Perkins, "Harmonic balance/Galerkin method for non-smooth dynamic systems," *Journal of Sound and Vibration*, vol. 261, no. 2, pp. 213–224, 2003.

[37] M. Krack and J. Gross, *Harmonic Balance for Nonlinear Vibration Problems*, Springer International Publishing, Cham, 2019.

[38] M. Nakhla and J. Vlach, "A piecewise harmonic balance technique for determination of periodic response of nonlinear systems," *IEEE Transactions on Circuits and Systems*, vol. 23, no. 2, pp. 85–91, 1976.